



HAL
open science

Nonadiabatic dynamics simulations of photoexcited urocanic acid

Deniz Tuna, Lasse Spörkel, Mario Barbatti, Walter Thiel

► **To cite this version:**

Deniz Tuna, Lasse Spörkel, Mario Barbatti, Walter Thiel. Nonadiabatic dynamics simulations of photoexcited urocanic acid. *Chemical Physics*, 2018, 515, pp.521-534. hal-01965450

HAL Id: hal-01965450

<https://amu.hal.science/hal-01965450v1>

Submitted on 26 Dec 2018

HAL is a multi-disciplinary open access archive for the deposit and dissemination of scientific research documents, whether they are published or not. The documents may come from teaching and research institutions in France or abroad, or from public or private research centers.

L'archive ouverte pluridisciplinaire **HAL**, est destinée au dépôt et à la diffusion de documents scientifiques de niveau recherche, publiés ou non, émanant des établissements d'enseignement et de recherche français ou étrangers, des laboratoires publics ou privés.



Distributed under a Creative Commons Attribution 4.0 International License

Summary
8/29/2018 1:55:32 AM

Differences exist between documents.

New Document:

[ua-om2mrci-tsh-dynamics-R1](#)

40 pages (6.88 MB)
8/29/2018 1:55:04 AM

Used to display results.

Old Document:

[ua-om2mrci-tsh-dynamics](#)

40 pages (6.88 MB)
8/29/2018 1:55:04 AM

[Get started: first change is on page 1.](#)


No pages were deleted

How to read this report

Highlight indicates a change.

Deleted indicates deleted content.

 indicates pages were changed.

 indicates pages were moved.

Nonadiabatic Dynamics Simulations of Photoexcited Urocanic Acid

Deniz Tuna^{a,1,*}, Lasse Spörkel^a, Mario Barbatti^b, Walter Thiel^a

^a*Max-Planck-Institut für Kohlenforschung, 45470 Mülheim an der Ruhr, Germany*

^b*Aix Marseille Univ, CNRS, ICR, Marseille, France*

Abstract

Urocanic acid (UA) is a UV filter found in human skin, which has been linked to photoimmunosuppression and the formation of skin cancer. Its UV-light-induced photoisomerization and radiationless deactivation mechanisms have been addressed previously by static calculations. In this paper, we present nonadiabatic trajectory-surface-hopping dynamics simulations of photoexcited UA using the semiempirical OM2/MRCI methodology and an adaptive-timestep algorithm. We have simulated almost 6000 trajectories, each for a simulation time of 1.6 ps, covering the entire conformational space of the *E* and *Z* isomers of both possible tautomers of the isolated neutral form of UA (overall 32 conformers). Initial conditions for the excited-state dynamics were obtained from 1 ns ground-state dynamics simulations. We find that UA has an ultrashort excited-state lifetime, which is due to ultrafast radiationless excited-state deactivation driven by $E \leftrightarrow Z$ photoisomerization and excited-state intramolecular proton-transfer (ESIPT) processes. The computed S_1 excited-state lifetimes for the *E* and *Z* isomers of the N1H and N3H tautomers range from 271 to 506 fs. The photoisomerization quantum yield is calculated to be 43% (32%) for the combined *E* (*Z*) isomers of both tautomers. The shorter lifetime and the lower photoisomerization quantum yield of the *Z* isomers can be rationalized by the larger number of available excited-state deactivation processes: the *Z* isomers can undergo ESIPT and

*Corresponding author

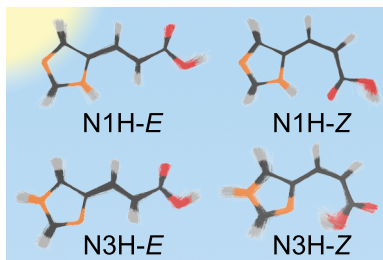
Email address: tuna@kofo.mpg.de (Deniz Tuna)

¹Author's current affiliations: Department of Chemistry and The PULSE Institute, Stanford University, Stanford, California 94305, United States; SLAC National Accelerator Laboratory, Menlo Park, California 94025, United States

photoisomerization, whereas the *E* isomers can only deactivate via the latter process. The intramolecular hydrogen bond that is present in many *Z* conformers can prevent successful photoisomerization to an *E* isomer. We find no evidence for an excitation-energy-dependent quantum yield for photoisomerization (EEDQY-PI) in isolated (*E*)-UA, which has previously been detected spectroscopically in aqueous solution. However, we do find an EEDQY-PI as well as a complementary excitation-energy-dependent quantum yield for ESIPT (EEDQY-ESIPT) for the N1H-*Z* isomers, which demonstrates the competition of the photoisomerization and ESIPT processes. The present comprehensive study lays the groundwork for future photodynamics simulations of UA in the aqueous phase.

Keywords:

UV photostability, UV filter, photoisomerization, excited state dynamics, excited state deactivation, nonadiabatic dynamics, trajectory surface hopping, conical intersection, semiempirical methods, quantum chemistry, excited state intramolecular proton transfer, ESIPT, photoisomerization quantum yield



Graphical abstract

1. Introduction

Urocanic acid (UA) is a naturally occurring UV chromophore. It is found in human skin, in the uppermost layer of the epidermis, the *stratum corneum*. The *E* isomer of UA is produced by the enzyme histidine ammonia-lyase acting on histidine. When (*E*)-UA absorbs UV light, it can undergo *E*→*Z* photoisomerization. This leads to a buildup of (*Z*)-UA in the upper layers of skin. A few decades ago, UA was believed to act as a UV filter and

thus as a natural sunscreen, but later evidence suggested that the *Z* isomer can suppress the immune system and through a complex mechanism might even facilitate the onset of skin cancer.[1] Over the last few decades, UA has attracted multidisciplinary interest in the fields of photochemistry, photobiology, spectroscopy, immunology, dermatology, biochemistry and bacteriology. Three reviews on various aspects of UA[1, 2, 3] and a comment[4] summarize relevant aspects of this molecule. UA has recently been the focus of study in a multitude of scientific fields such as macromolecular chemistry, transition-metal chemistry, genetics, medicine and dermatology.[5, 6, 7, 8, 9, 10, 11, 12]

Spectroscopic and kinetic studies on UA in aqueous solution are available in abundance.[13, 14, 15, 16, 17, 18, 19, 20, 21, 22, 23, 24, 25] Probably the most important result of these studies is the identification of a wavelength-dependent quantum yield for $E \rightarrow Z$ photoisomerization.[13, 17] In contrast, we are aware of only a single spectroscopic investigation on isolated UA that reported its fluorescence excitation and fluorescence emission spectra in a supersonic jet.[26]

UA has also been a popular subject in computational chemistry.[27, 28, 29, 30, 31, 32, 33, 34, 35, 36, 37, 38, 39, 40, 41] Early studies focused on the relative energies of the different tautomers and isomers.[29, 30] The conformational dynamics in aqueous solution were explored by molecular dynamics (MD) simulations.[35] Vertical excitation energies were reported for various species and protonation states of UA.[27, 31, 32, 33, 34, 40, 41] Static computational studies on the photoreactivity of UA focused on photosensitization (triplet-excited UA can react with 3O_2 to produce 1O_2),[38] on hydroxyl-radical scavenging[39] and on photoisomerization.[36, 37, 41]

In aqueous solution, (*E*)-UA exhibits an excitation-energy-dependent quantum yield for photoisomerization (EEDQY-PI). When UA is excited at the red tail of the absorption spectrum around 310 nm (4.0 eV), the $E \rightarrow Z$ photoisomerization quantum yield is at its maximum of 50%. When it is excited at the blue maximum of the absorption spectrum around 265 nm (4.68 eV), the $E \rightarrow Z$ photoisomerization quantum yield is at its minimum of 5%.[13, 17] Several explanations for this effect have been proposed over the last 20 years, **i.e.** different rotamers in the ground state,[27] a manifold of excited states,[15, 16, 17, 2] different tautomers in the ground state,[40] different energy windows for exciting the bright $\pi\pi^*$ state and the different order of $n\pi^*$ and $\pi\pi^*$ states in the two tautomers.[41] An open question is whether this effect can be observed only in the condensed phase or also in isolated UA.

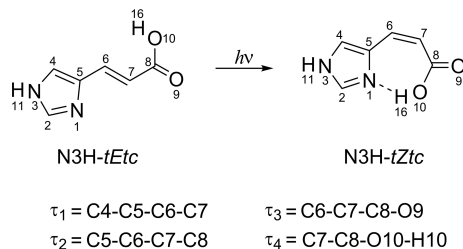


Figure 1: Structural formulas (including atom numbers) of a conformer of the N3H tautomer of UA and its photoisomerization product. The designations of the isomers used in this work are given below the structures. The four relevant torsion angles defining the tautomers, isomers and conformers are given at the bottom.

Figure 1 shows the structural formulas of the *E* and *Z* isomers of one conformer of the N3H tautomer of UA as well as the four dihedral angles used to distinguish the different isomers and conformers. The notation used in this work was introduced in a previous study[41] and is briefly described again here. The prefix before the dash specifies the protonation site of the imidazole moiety (N1H or N3H), i.e. the tautomeric form. The suffix after the dash denotes the torsion angles of the four relevant bonds. Three of these are single bonds, which are characterized by the descriptors “*t*” for “*trans*” and “*c*” for “*cis*”. The descriptors “*E*” and “*Z*” specify the torsion angle of the isomerizing C=C bond. The isomer N3H-*tEtc*, for example, is protonated at the N3 position of the imidazole moiety and exhibits a C4–C5–C6–C7 torsion angle of $\sim 180^\circ$ (*t*), a C5–C6–C7–C8 torsion angle of $\sim 180^\circ$ (*E*), a C6–C7–C8–O9 torsion angle of $\sim 180^\circ$ (*t*) and a C7–C8–O10–H10 torsion angle of $\sim 0^\circ$ (*c*). Upon photoisomerization, the N3H-*tZtc* isomer is formed. This example is shown in Figure 1.

The semiempirical orthogonalization-corrected OM2 (orthogonalization model 2) method goes beyond the MNDO (modified neglect of diatomic overlap) model of the NDDO (neglect of diatomic differential overlap) approximation by including explicit orthogonalization corrections into the one-electron Hamiltonian.[42, 43, 44] This remedies many problems resulting from the shortcomings of the MNDO model and lays the groundwork for the development of a method that can be applied for realistic computations of electronically excited states. The semiempirical self-consistent-field (SCF) solution serves as the reference for a multireference configuration interaction (MRCI) treatment, which can be applied to species with strong multireference character and to electronically excited states.[45, 46]

Based on previous static explorations of photochemical reaction paths,[41] photoisomerization and excited-state intramolecular proton transfer (ESIPT) are the main photoinduced processes expected to be of significance for the excited-state dynamics in UA. These two types of photoreactions have been studied extensively with computational methods in the past.[47, 48, 49, 50, 51, 52, 53, 54] In the present work, we report on a comprehensive nonadiabatic MD study initiated in the low-lying electronically excited states of isolated UA. The dynamics simulations employ the semiempirical OM2/MRCI method[45, 43, 44] and Tully’s fewest-switches trajectory-surface-hopping (TSH) approach.[55, 56, 57, 58, 59] The OM2/MRCI method has been successfully applied in many recent excited-state TSH studies of medium-size organic chromophores.[43, 46, 60, 61, 62, 63, 64] In the present study, we focus on the excited-state lifetimes and on the competition between photoisomerization and ESIPT processes in the various tautomers, isomers and conformers of UA, and we also ascertain whether the simulations provide any evidence of an EEDQY-PI being present in isolated UA.

2. Computational Methods

The MNDO99 program was used for the OM2/SCF and OM2/MRCI calculations.[65] Vertical excitation energies were computed at the OM2/MRCI level using the previously published ground-state equilibrium geometries of eight selected *E* and *Z* isomers of both UA tautomers.[41] These structures had been optimized with the second-order Møller-Plesset (MP2) method and the cc-pVDZ basis set (MP2/cc-pVDZ) without imposing any symmetry restrictions using the Turbomole 6.3.1 program package.[66]

For the OM2/MRCI calculations of vertical excitation energies and the simulation of the TSH dynamics, we adopted a (12,10) active space comprising eight π MOs (4 occupied, 4 unoccupied) and two occupied *n* MOs. This active space covered both the lowest-lying $n\pi^*$ state (involving the n_O lone-pair MO at the acid moiety, usually S_1 or S_2) and the second higher-lying $n\pi^*$ state (involving the n_N MO at the imidazole moiety, usually S_4 or higher). A visual presentation of the MOs comprising the (12,10) active space is shown in Figure S1 in the Supporting Information for the N3H-*tEct* isomer. For many molecular conformations, especially in the N3H tautomer, the two relevant lone-pair MOs are strongly localized on either the nitrogen atom of the imidazole ring or the oxygen atom of the acid moiety as well as clearly separated in energy. In other conformations they undergo strong

mixing and are almost equal in energy (especially in the N1H tautomer, see Fig. S2 in the Supporting Information for a visual presentation of the two lone-pair MOs of the N1H-*tEct* isomer). For these reasons, it is advisable to include both lone-pair MOs in the active space to ensure a balanced treatment. With this choice, the active space contains a contiguous block of the six highest occupied MOs, that is, HOMO to HOMO-5.

For preparing the initial conditions for the excited-state dynamics simulations, we ran self-consistent-charge density functional tight binding (SCC-DFTB) ground-state dynamics simulations with ChemShell 3.5.0[67, 68] using a timestep of 1 fs, an NVT ensemble and a Nosé-Hoover-chain thermostat of chain-length 10 at 300 K with a characteristic timestep of 0.05. An initial equilibration run of 2 ps was followed by a production run of 1 ns.

During the TSH simulations, we employed the half-electron restricted open-shell Hartree-Fock (ROHF) formalism for all OM2/SCF calculations preceding the OM2/MRCI calculations. The ROHF MOs were optimized for a configuration with two singly occupied MOs (HOMO and LUMO of the closed-shell configuration). This provides a better description of multiconfigurational situations like S_1/S_0 conical intersections (with biradical character) that play an essential role in excited-state dynamics simulations. For the MRCI treatment, three configuration state functions were chosen as references, namely the ROHF SCF configuration and the two closed-shell configurations derived therefrom (i.e., all singlet configurations that can be generated from HOMO and LUMO of the closed-shell ground state). The MRCI wave function was built by allowing all single and double excitations from these three references.

For the nuclear propagation of the TSH dynamics under NVE conditions, we used a regular timestep of 0.2 fs. The timestep for the integration of the electronic Schrödinger equation was 0.001 fs. The fewest-switches criterion for surface hopping[55] was applied to all points along the trajectory with an energy gap between adjacent electronic states of less than 10 kcal/mol. An empirical decoherence correction of 0.1 a.u. was used.[69]

The simulations employed the recently proposed adaptive-timestep algorithm for stabilizing the OM2/MRCI excited-state dynamics.[70] This algorithm is applied whenever a trajectory encounters a region with active-space problems, i.e. when there is strong mixing or even switching of active and inactive MOs; in such cases, the timestep for the propagation of the nuclear dynamics is successively halved until the problematic region has been left behind, after which the timestep is restored to its original value. The use of



this algorithm leads to a significantly lower number of unsuccessful trajectories and, more importantly, ensures that the total energy stays constant during long simulations. We adopted the following criteria: the timestep was adapted when the total energy changed by more than 0.0001 kcal/mol, or when the overlap of active MOs was less than 0.97 between consecutive timesteps of the nuclear propagation. \blacktriangle

We propagated four batches of excited-state trajectories for the four classes of isomers and performed our standard post-processing to filter out any problematic trajectories. The first post-processing procedure removes trajectories that exhibit sudden energy jumps between two consecutive timesteps of more than 5 kcal/mol. The second filter checks whether a trajectory has run for the requested number of steps; if not, it is rejected unless the system has already remained in the S_0 state for at least 50 fs. In this latter case, it has successfully completed the radiationless deactivation to the ground state and can therefore be included in the principal photochemical analysis. The second filter thus avoids discarding trajectories that exhibit proper excited-state dynamics and abort for technical reasons well after hopping to the ground state (e.g. by visiting unusual ground-state structures).

Excited-state lifetimes of the S_2 and S_1 states were fitted with a mono-exponential decay function of the form

$$p(t) = Ae^{-(t-\tau_d)/\tau_e} + p_0 \quad (1)$$

where τ_e is the fitted decay time of the excited state, τ_d is the initial delay time that corresponds to the time between first population of an excited state and the onset of its population depletion via internal conversion to a lower state, A is the amplitude and p_0 is the fraction of trajectories that remain in the excited state at the end of the simulation time. The reported excited-state lifetime is the sum $\tau = \tau_e + \tau_d$.

3. Results

3.1. Validation of OM2/MRCI

Before initiating excited-state dynamics simulations, we need to ensure that OM2/MRCI is able to correctly describe the low-lying excited states of UA. For this purpose, we computed the OM2/MRCI vertical excitation energies (VEEs) at the ground-state MP2/cc-pVDZ equilibrium geometries of eight selected conformers of the E and Z isomers of the N1H and N3H tautomers and compared them with published MS-CASPT2 and CC2 values.[41]

The current OM2/MRCI and the previous MS-CASPT2 calculations employed the same (12,10) active space comprised of two occupied lone-pair MOs and four occupied and four unoccupied π MOs (see Computational Methods).

The VEEs from OM2/MRCI and those from MS-CASPT2 and CC2[41] are listed in Table S1 of the Supporting Information. In the case of the S_1 and S_2 states, the OM2/MRCI and *ab initio* results generally agree well (typically within 0.2 eV). These two states lie close to each other and their order ($n\pi^*$ vs. $\pi\pi^*$) varies in the set of the eight selected conformers. OM2/MRCI and MS-CASPT2 agree in the predicted order in all eight cases, hence the physical nature of the S_1 and S_2 states is correctly reproduced by OM2/MRCI. For the S_3 , S_4 and S_5 states, there are some larger deviations between the OM2/MRCI and *ab initio* results, with a tendency of OM2/MRCI to underestimate the corresponding VEEs. Our dynamics study involves only the lowest three singlet excited states; most relevant are the lowest two which are well described by OM2/MRCI.

In summary, the use of OM2/MRCI for excited-state dynamics simulations of UA appears to be justified by the validation for the lowest $n\pi^*$ and $\pi\pi^*$ states (S_1 and S_2), in particular with regards to the state ordering. We note that the conical-intersection seam[71, 72] mediating S_1/S_0 deactivation via torsional motion around the central double bond is of $\pi\pi^*/S_0$ type, as in any ethylene derivative.[73] Therefore, the approach toward this conical-intersection seam will be accompanied by a decrease in energy of the $\pi\pi^*$ state. In conformers where the bright $\pi\pi^*$ state is the S_2 state, a slight torsional motion of the molecule is thus expected to cause a switch in the energetic order of the $n\pi^*$ and $\pi\pi^*$ states.[41] Further evidence that the topography of the $n\pi^*$ and $\pi\pi^*$ states connecting the *E* and *Z* isomers along the photoisomerization coordinate is correctly described by the OM2/MRCI method will be presented later.

3.2. Tautomers, Isomers and Conformers: Sampling of the Conformational Space via Ground-State Dynamics Simulations

For both N1H and N3H tautomers of UA, we consider the *E* and *Z* isomers with respect to the central C=C double bond. For each of these isomers, eight different rotamers/conformers exist, as each of the three defining single bonds τ_1 , τ_3 and τ_4 (see Fig. 1) can have either *trans* or *cis* conformation, resulting in $2^3 = 8$ rotamers/conformers. For each of these eight species, we performed a 1 ns ground-state MD simulation, resulting in a total of 32

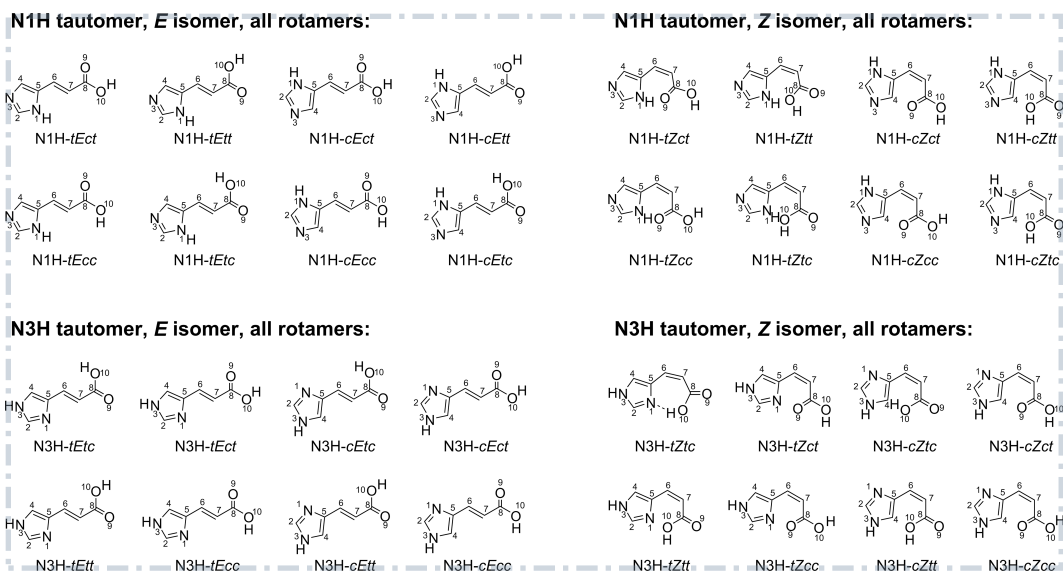


Figure 2: Structural formulas of the 32 conformers of UA (each assigned to one of the four “isomer classes” used throughout this work) that were considered as starting structures for the ground-state MD simulations, which were used for the generation of the initial conditions for the excited-state MD simulations. The nomenclature and atom numbering used throughout this work is given as well. An SCC-DFTB ground-state dynamics simulation of 1 ns length was initiated for each of these conformers. From each of these ground-state MD trajectories 250 geometries were randomly extracted, yielding 2000 starting structures for each of the four classes of isomers and 8000 starting structures in total.

MD simulations starting from all possible conformers of this molecule. All 32 possible rotamers and their connection to the *E* and *Z* isomers of the N1H and N3H tautomers are shown in Figure 2. Each ground-state MD simulation was run for 1 ns to ensure that a large number of rotamerizations (i.e. internal rotations around the three flexible single bonds) can take place so that each *E* and *Z* isomer is properly equilibrated with respect to all possible rotamers. This was done to avoid any unjustifiable bias in favor of less stable rotamers. In fact, highly unstable rotamers are found to rotamerize almost instantly after the start of the ground-state MD simulation and never reform. Rotamers of medium stability remain present for a longer time (e.g. 100–500 ps) before rotamerizing. Highly stable rotamers, on the other hand, do not rotamerize during the 1 ns simulation and are in addition formed by internal rotations in other trajectories, which were started from less stable rotamers. As a consequence, highly unstable rotamers are practically never

Table 1: Initial conditions for the excited-state MD trajectories: for each of the four classes of isomers (i.e. for the E and Z isomers of the N1H and N3H tautomers, respectively) 2000 structures were randomly sampled from the eight ground-state trajectories initiated from the different conformers of each isomer class (32 conformers and trajectories in total). These 2000 sampled structures per class (8000 in total) were subjected to a filtering procedure (see text). This table lists how many structures passed this procedure and how many of these populate a given excited state with the corresponding initial conditions for the excited-state MD simulations. Also shown are the number of successful excited-state trajectories that passed all post-processing filters after completion of the TSH dynamics.

state	N1H tautomers		N3H tautomers	
	E isomers	Z isomers	E isomers	Z isomers
S_1	1422	1354	1179	954
S_2	32	61	186	261
S_3	38	60	169	210
sum	1492	1475	1534	1425
successful TSH				
trajectories	1380	1423	1474	1352

sampled for the initial conditions of the excited-state dynamics simulations, whereas highly stable rotamers are sampled in large numbers.

We carried out the ground-state MD simulations using the SCC-DFTB method.[74] SCC-DFTB was preferred over OM2/SCF because it better reproduced the DFT(B3LYP)/TZVP results for the relative stability of two crucial conformers of UA, N3H-*tZtc* and N3H-*cZct* (see Fig. 2).[40] Further details on this are given in the Supporting Information.

From each of the eight ground-state MD simulations conducted for the E or Z isomers of each of the two tautomers (i.e. for one “block” as shown in Figure 2), we randomly sampled 250 geometries. The resulting 2000 sampled geometries were collected and subjected to a filtering procedure.[75] This procedure involves OM2/MRCI single-point calculations of the vertical excitation energies and oscillator strengths at each of the 2000 sampled geometries. From these data a transition probability was computed and then compared to a random number[75] to decide whether that geometry is kept, and if so, in which of the considered excited states to initiate the nonadiabatic dynamics. This procedure thus generates the excited state(s) at each sampled geometry most likely to be populated by optical absorption. The numbers of passed trajectories for each of the four batches of trajectories (E and Z isomers of N1H and N3H tautomers, respectively) split up into the

different initially populated excited states, are given in Table 1. It is evident that our filtering procedure preferentially generates the strongly absorbing $S_1(\pi\pi^*)$ state, whereas the weakly absorbing $S_2(n\pi^*)$ and $S_3(\pi\pi^*)$ states are populated only sparsely (see also Table S1 in the Supporting Information). In the N1H tautomers, the S_1 state is dominating even more than in the N3H tautomers. In total, the processing of each of the four batches resulted in 1425–1534 initial conditions (i.e. structures, velocities, initially populated states), which served as starting points for the excited-state dynamics simulations. The initial structures are shown as an overlay in Figure 3.

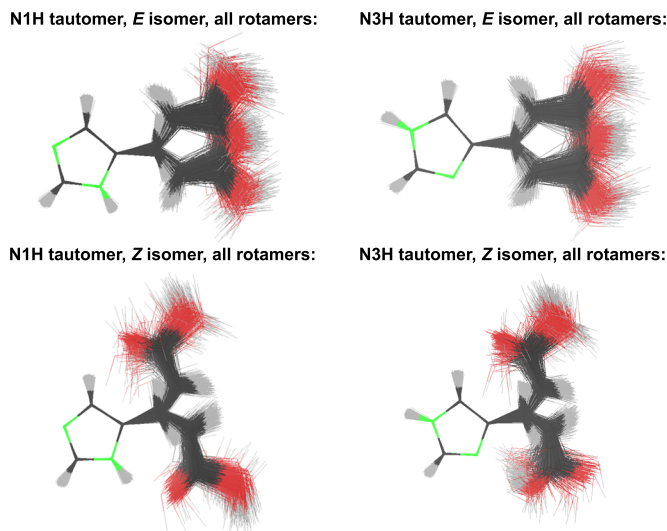


Figure 3: Overlay of all starting structures used as part of the initial conditions for the excited-state dynamics simulations of the four batches of trajectories. The structural alignments were centered on the imidazole ring. These overlays comprise (starting from the top left and continuing clockwise) 1492, 1534, 1425 and 1475 structures (see Table 1).

In Figure S3 of the Supporting Information, we present the range of the vertical excitation energies for each of the initially populated states, or in other words, the energy initially pumped into the system at the beginning of each excited-state trajectory. In the energy window of very low excitation energies of < 4 eV, we mainly excite the S_1 state of the N1H- Z species (with a very minor proportion of N3H- Z species). The excitation of the E isomers of both tautomers requires energies of > 4 eV (N1H) or > 4.25 eV (N3H). For excitation to the S_2 and S_3 states, all four classes of isomers exhibit roughly the same energy windows, i.e. S_2 4.50–5.35 eV and S_3 4.75–5.60 eV. These

data confirm earlier findings that both the E and Z isomers of the N1H tautomer can be excited at lower energies than those of the N3H tautomer.[41] To visualize the distribution of the initial excitation energies throughout the many starting structures, Figure S4 in the Supporting Information shows histograms of the vertical excitation energies of the initially populated state for each starting structure. The isomers of the N1H tautomer exhibit one “absorption band” with a very weak tail, whereas the N3H tautomer shows a shoulder toward higher excitation energies for the E isomers and two sizable bands for the Z isomers. Hence, the excited-state trajectories of the N1H tautomer start with excitation energies of mainly 3.70–4.70 eV, whereas the trajectories of the N3H tautomer can also carry larger excitation energies of 4.70 eV upwards. (We should point out that the histograms shown in Figure S4 are not properly simulated absorption spectra, because only the initially populated excited state of each starting structure is considered.)

3.3. Surface-Hopping Dynamics Simulations

In the following, we will present the results of almost 6000 excited-state trajectories. We focus on the excited-state lifetimes, the dynamics of the radiationless deactivation mechanisms and the competition between these mechanisms.

3.3.1. Excited-State Lifetime

Figure S5 of the Supporting Information shows histograms of the S_1/S_0 hopping times for the four batches of trajectories. The E isomers of the N1H tautomer deactivate faster than the E isomers of the N3H tautomer. For the Z isomers it is the other way around. The Z isomers of the N3H tautomer deactivate the fastest.

Figure 4 shows the average state populations, the fit of the monoexponential decay of the S_2 and S_1 populations and the computed excited-state lifetimes of S_2 and S_1 ; the lifetime of S_3 is negligibly short. These data quantify the observations made by inspection of Figure S5: the Z isomers of the N3H tautomer deactivate the fastest with an S_1 lifetime of only 271 fs (+ 22 fs for S_2). The E isomers of the N1H tautomer deactivate faster than the E isomers of the N3H tautomer (408 vs. 506 fs). The Z isomers of the N3H tautomer deactivate significantly faster than the corresponding E isomers (271 vs. 506 fs), whereas in the N1H tautomer, the difference between Z and E isomers is less pronounced (337 vs. 408 fs). The N1H- Z isomers, however, show an unusually long S_2 lifetime of 57 fs. It is also interesting to note that

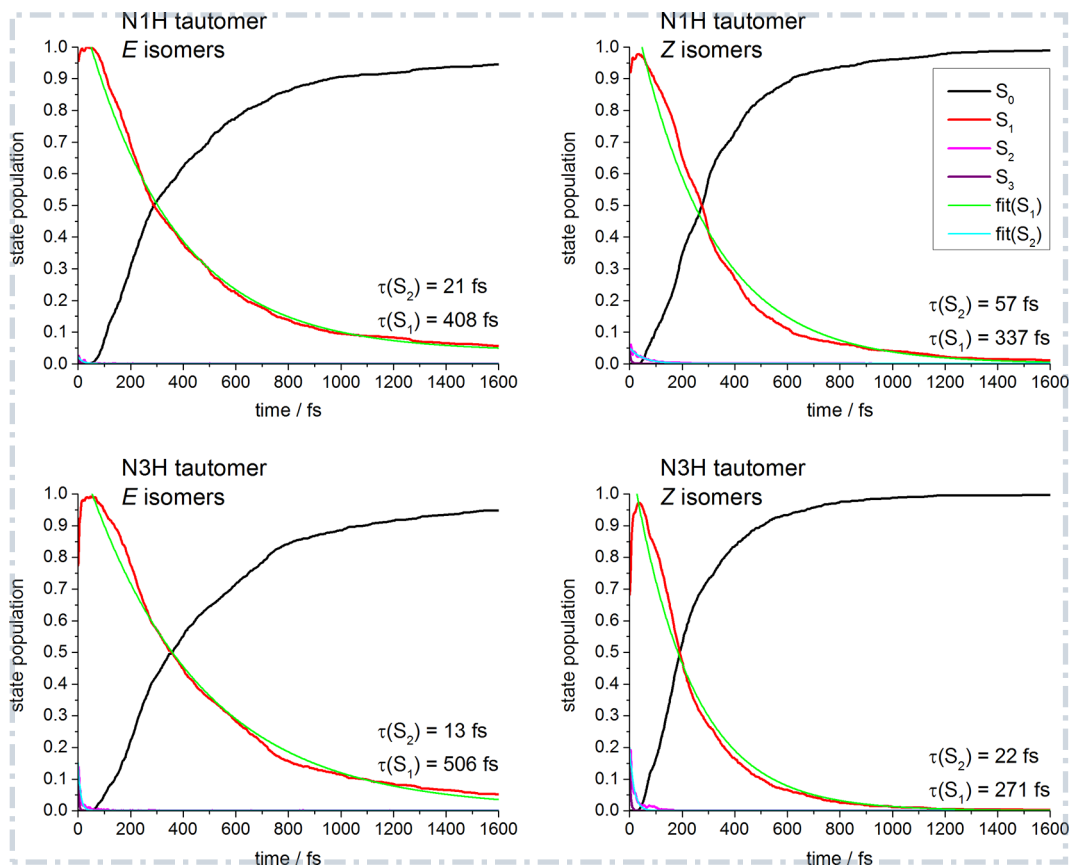


Figure 4: Average state populations of S_0 – S_3 (black, red, magenta, purple) for the four batches of trajectories collecting the starting geometries of all conformers of a given isomer and a given tautomer. The depletions of the S_2 and S_1 state populations were fitted with a monoexponential decay function (cyan and green, see text for details). The computed excited-state lifetimes of S_2 and S_1 (i.e. the sum of the initial delay time and the fitted decay time of S_2 and S_1) are printed in the lower right corner.

the S_1 populations of the E isomers of both tautomers do not decrease to 0, but instead reach plateau values of 0.06 for N1H- E and 0.05 for N3H- E after the simulation of 1.6 ps.

We have combined the data for the E isomers of the N1H and N3H tautomers (see Fig. S6 of the Supporting Information) and computed their excited-state lifetime, which yields 459 fs for S_1 (14 fs for S_2). We have done the same for the Z isomers of both tautomers and obtained an S_1 lifetime of 307 fs (30 fs for S_2). Finally, for a complete mixture (both E and Z isomers

of both N1H and N3H tautomers) the computed lifetime is 373 fs for S_1 (22 fs for S_2).

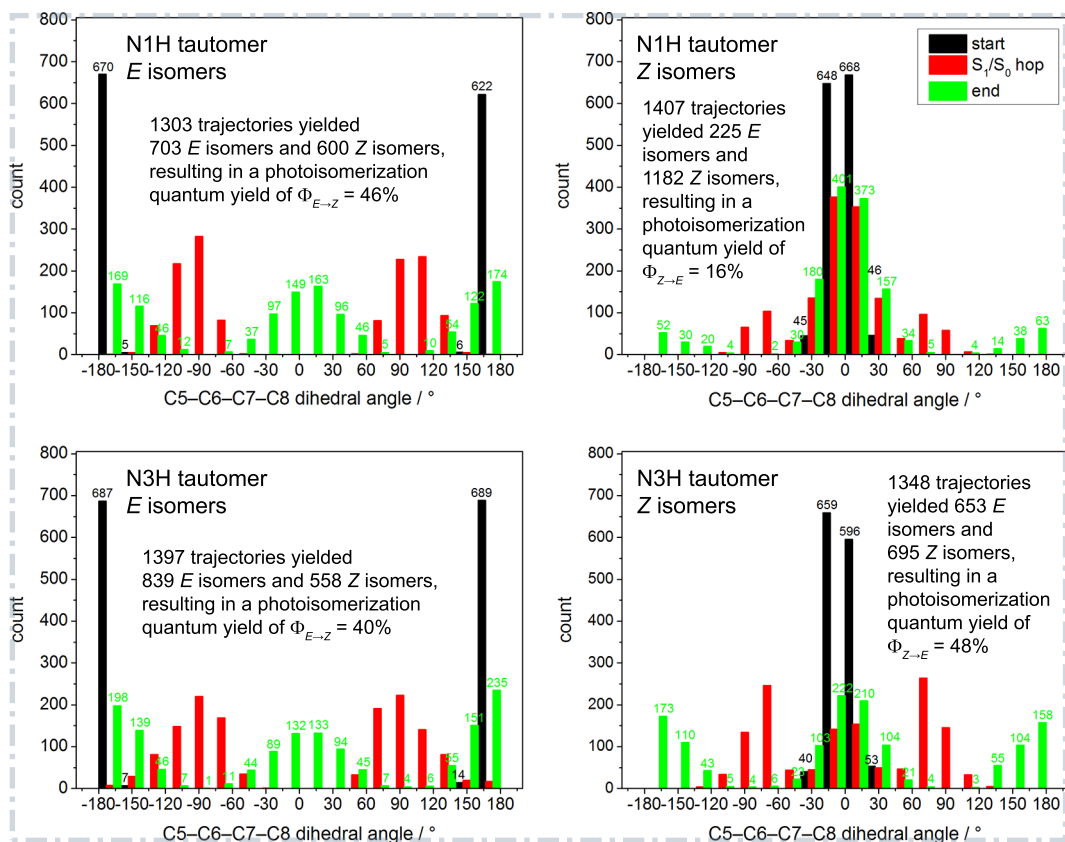


Figure 5: Histograms of the central dihedral angle at the starting geometry (black), the S_1/S_0 hopping point (red) and the final geometry (green) of each trajectory. The analysis was performed separately for each of the four classes that collect the conformers of a given E or Z isomer of a given tautomer. The photoisomerization quantum yield was computed based on the counts of E and Z isomers at the beginning and at the end of each trajectory (numbers on top of each bar). The quantum yield for photoisomerization is computed to be 43% (32%) for the combined E (Z) isomers of both tautomers (see text within the plots for details).

3.3.2. Photoisomerization

Figure 5 presents histograms of the central dihedral angle at three crucial points of the dynamics simulations, i.e. the starting geometries, the S_1/S_0 hopping points and the final geometries of the trajectories. As shown in a previous static study on UA,[41] the optimized S_1/S_0 conical intersections that

drive the photoisomerization process exhibit a central dihedral angle of $\sim 90^\circ$ and a symmetrical topography with respect to the two “sides” of the lower potential-energy surface (PES) (connecting the ground-state potential-energy wells of the E and Z minima). They should therefore mediate a successful photoreaction, i.e. a photoisomerization, or an aborted photoreaction, i.e. a return to the ground-state reactant with retention of the configuration, at roughly equal probability. Not surprisingly, the dihedral angle encountered at the S_1/S_0 hopping points is given by a Gaussian distribution around the value of 90° .

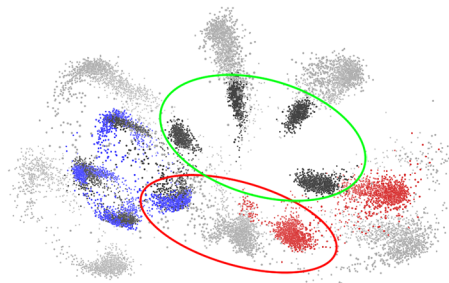


Figure 6: Overlay of the S_1/S_0 hopping points of the Z isomers of the N1H tautomer (1407 structures in total): only the nuclei are shown as dots. The red ellipse marks the region of the intramolecular hydrogen bond between the NH or CH group of the imidazole ring and the oxygen atom of the acid moiety. The green ellipse marks the region of the central C5–C6–C7–C8 moiety, with a dihedral angle mostly in the range between -60 and 60° due to the intramolecular hydrogen bond.

We first discuss the photoisomerization of the Z isomers. Upon irradiation, the Z isomers of the N1H tautomer rarely undergo isomerization but mainly deactivate back to the reactant. This is clearly seen in the histograms for the starting and final geometries (Fig. 5), which show peaks for the central dihedral angle close to 0° ; maybe more surprisingly, many of the corresponding hopping points also have small dihedral angles and the expected values of around $\pm 90^\circ$ are encountered quite rarely. For the N1H- Z isomers, even the hopping points have their maxima around 0° ; for the N3H- Z isomers the maxima are found around $\pm 75^\circ$. Inspection of all S_1/S_0 hopping points of the batch of trajectories for the Z isomers of the N1H tautomer (Fig. 6) rationalizes this finding: most of the hopping points contain a hydrogen bond between the imidazole and the acid moieties of the molecule, which is marked by the red ellipse in Figure 6. Such hydrogen bonds strongly stabilize the

Z form and trap the molecule in a structure with a central dihedral angle not far from 0° (marked by the green ellipse in Fig. 6). Hence, the molecule only rarely breaks free from these hydrogen bonds during the dynamics. In many trajectories, the central part of the molecule moves toward the S_1/S_0 conical-intersection seam for isomerization, against the restraint of the **intra**molecular hydrogen bond. This seam is encountered in the region around $\pm 60^\circ$ where internal conversion to the ground state with retention of configuration becomes feasible. Under the restraint of the intramolecular hydrogen bond, it is very difficult to reach the crossing region around $\pm 90^\circ$, hence the likelihood of forming the *E* isomer as the photoproduct is very low. By contrast, in the *Z* isomers of the N3H tautomer there must be significantly less propensity to such intramolecular hydrogen bonding or these hydrogen bonds are less stable—details on this will be presented below—hence the S_1/S_0 hopping points show a more Gaussian-like shape closer to $\pm 90^\circ$. Consequently, the *Z* isomers of the N3H tautomer yield significantly more *E* photoproduct than the *Z* isomers of the N1H tautomer. As a sidenote, it has to be pointed out that in many trajectories with a central dihedral angle around $\pm 0^\circ$ at the hopping point the isomerization process is not at all responsible for the nonadiabatic event, but instead an excited-state intramolecular proton transfer (ESIPT) is active. This type of deactivation process, which competes with the photoisomerization process in the *Z* isomers, entails that the central dihedral angle undergoes only minor changes during the nonadiabatic event, because the molecular motion driving the nonadiabatic transition is a proton transfer. This is demonstrated in Figure S7 in the Supporting Information, which shows that the central dihedral angle is found close to 0° when the ESIPT mechanism is responsible for the S_1/S_0 surface hop. We will discuss the ESIPT process in detail in the next subsection.

Figure 5 also reports on the quantum yields for photoisomerization, but this aspect will be discussed in more detail in a later subsection.

Figure 7 shows the time evolution of the central C5–C6–C7–C8 dihedral angle of 200 randomly selected trajectories of the *E* isomers of the N3H tautomer. As already mentioned, the deactivation from S_3 and S_2 to S_1 takes at most 25 fs (with the exception of the N1H-*Z* isomers). Hence, the red parts of the trajectories essentially evolve on the S_1 PES, whereas the green parts evolve on the S_0 PES. In contrast to the *Z* isomers discussed above, the *E* isomers show only one dominating mechanism for excited-state deactivation, i.e. $E \rightarrow Z$ photoisomerization. The molecule begins to initiate the photoisomerization motion mostly within 150 fs after excitation and it

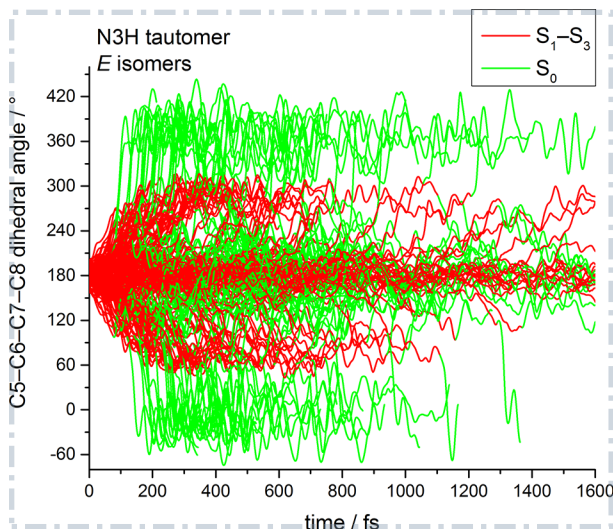


Figure 7: Time evolution of the central C5–C6–C7–C8 dihedral angle of the *E* isomers of the N3H tautomer for 200 randomly selected trajectories. Red and green lines depict the parts of the trajectories evolving on an excited state (S_1 – S_3) and on the ground state (S_0), respectively.

reaches the conical-intersection seam around $\pm 90^\circ$ about 100 fs after excitation or later. During the evolution in the S_1 state, the central dihedral angle changes by roughly $\pm 90^\circ$ until the S_1/S_0 intersection seam is reached. At the S_1/S_0 seam, the majority of trajectories deactivate to S_0 . Thereafter, the central dihedral angle evolves further to ~ 0 or 360° and thus to a *Z* isomer, or it reverts back to 180° and restores the *E* configuration. Part of the trajectories retain a dihedral angle around 180° throughout the dynamics run and an even smaller part remains in the S_1 state until the end of the 1.6 ps simulation. Finally, all trajectories that aborted before the end of the intended runtime had populated the S_0 state for at least 50 fs, consistent with the cutoff value adopted in our filtering procedure (see Computational Methods).

We mention at this point that we also observed a rare side process, i.e. a ring-opening/ring-breaking reaction. This is documented in Figure S8 of the Supporting Information.

As a last point in this subsection on the photoisomerization reaction, we present further evidence that OM2/MRCI correctly reproduces the nature of the low-lying excited states along the photoisomerization coordinate. Figure 8 shows a plot of the instantaneous energies of the closed-shell (black sym-

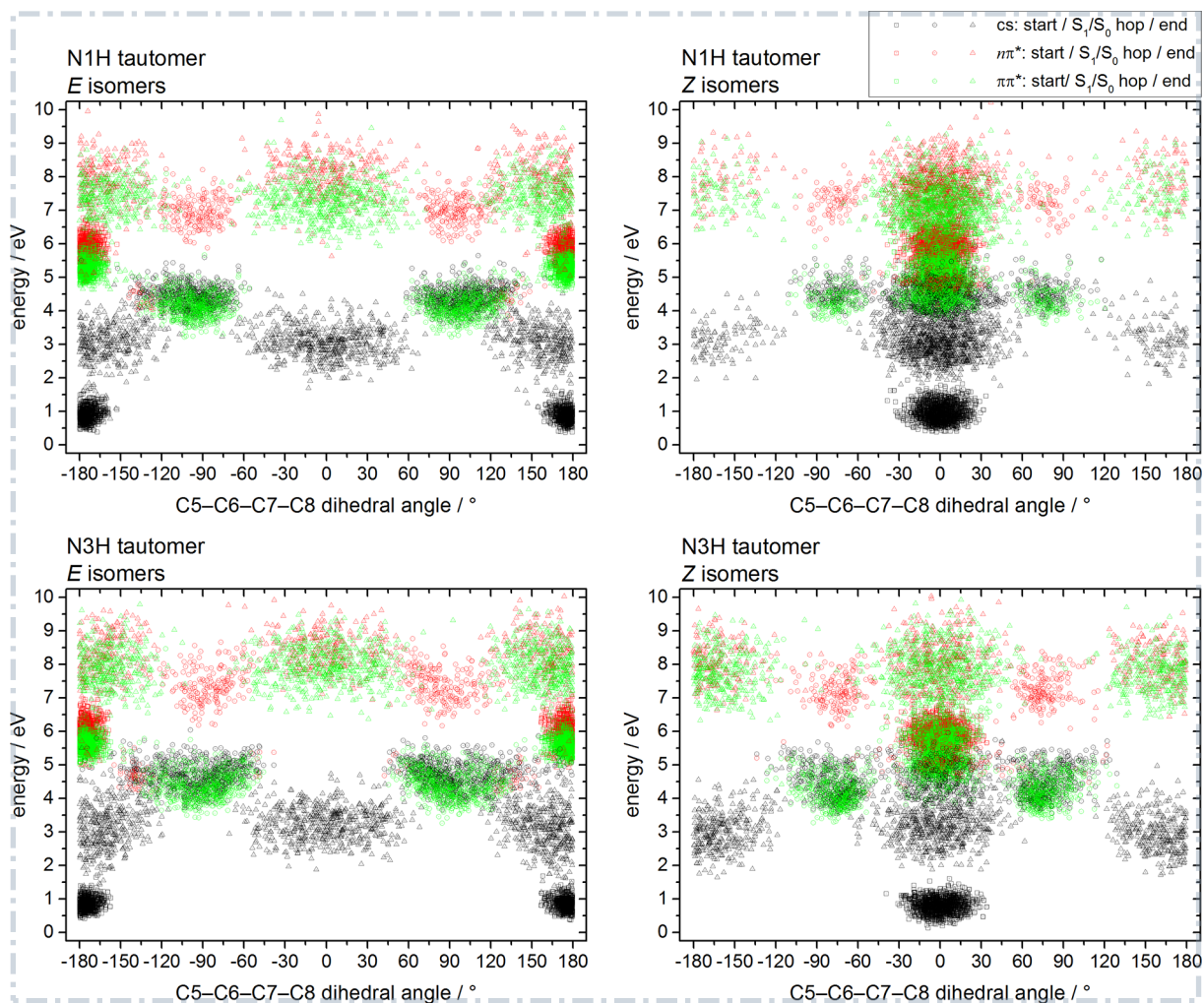


Figure 8: Dynamical reconstruction of the critical points on the PESs of UA along the photoisomerization coordinate. Plotted are the instantaneous energies of the closed-shell (black symbols), $n\pi^*$ (red) and $\pi\pi^*$ (green) diabatic states at the starting geometry (square symbols), the S_1/S_0 hopping point (circles) and the final geometry (triangles) of each trajectory. The energies are given relative to the OM2/MRCI S_0 energies of the lowest-energy conformer of each tautomer/isomer class, i.e. each plot has its own relative energy scale.

bol), $n\pi^*$ (red) and $\pi\pi^*$ (green) diabatic states for the critical points along the trajectories. These are the starting geometry (square symbols), the S_1/S_0 hopping point (circles) and the final geometry (triangles) of each trajectory.

This plot confirms in a dynamical context the static picture explored in a previous *ab initio* study on the photoisomerization of the N3H-*tEtc* and N3H-*tEct* conformers (see Figs. 2 and S2 of ref. 41), in which the diabatic state order was found to be closed-shell, $n\pi^*$, $\pi\pi^*$ in the planar *E* and *Z* minima and closed-shell, $\pi\pi^*$, $n\pi^*$ at the S_1/S_0 conical intersections. This scenario is confirmed by Figure 8 for the *E* isomers of the N3H tautomer. For the starting and final geometries (clusters of squares and triangles, respectively), the $n\pi^*$ state is the S_1 state and the $\pi\pi^*$ state is the S_2 state for geometries that are planar or close to planar. As soon as the molecule is distorted strongly enough from the planar configuration, the $\pi\pi^*$ state is shifted down in energy and becomes S_1 . In the present dynamics study, most starting geometries show an out-of-plane displacement, which is why they can show the reverse $S_1(\pi\pi^*)$, $S_2(n\pi^*)$ sequence. It is evident that each S_1/S_0 hopping point (clusters of circles) is part of a $\pi\pi^*/$ closed-shell conical-intersection seam with dihedral angles around $\pm 90^\circ$ (clusters of circles) and that the $n\pi^*$ state lies energetically well above this seam. In summary, the OM2/MRCI dynamics simulations yield a state order that is consistent with the available *ab initio* results at the minima and conical intersections,[41] but it can change at significantly distorted geometries that are visited during the simulations.

Analogous plots were generated for the other three classes of isomers (see Figure 8). We note briefly that the results for the N3H-*Z* isomers show the same trends as described above. In the case of the N1H tautomer, the previous static *ab initio* study placed the $n\pi^*$ state above the $\pi\pi^*$ state even for the planar *E* and *Z* minima,[41] which is also confirmed by our OM2/MRCI dynamics data.

3.3.3. Excited-State Intramolecular Proton Transfer

Why do the *Z* isomers deactivate faster than the *E* isomers? The only deactivation mechanism accessible to the *E* isomers of both tautomers is photoisomerization (apart from a very rare side reaction involving ring opening). As already mentioned above, this process can have two outcomes: retention of the configuration of the central double bond, i.e. aborted photoreaction ($E \rightarrow E$ or $Z \rightarrow Z$), or isomerization, i.e. successful photoisomerization ($E \rightarrow Z$ or $Z \rightarrow E$). A second deactivation mechanism was observed only in the *Z* isomers, namely the previously predicted ESIPT process.[41] ESIPT is known to be ultrafast in many similar systems[76, 77, 53, 78, 79, 80] and is thus expected to accelerate the deactivation of the photoexcited *Z* isomers. Finally, the ring-puckering deactivation process inherent to the imidazole moiety that

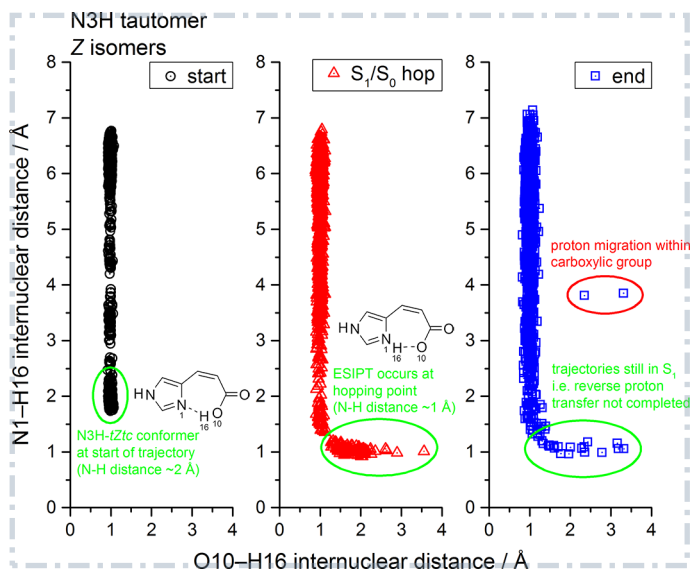


Figure 9: ES IPT process in the N3H-*tZtc* conformer, in which the proton is transferred from the OH group of the acid moiety to the nitrogen atom of the imidazole moiety. The three plots show the distribution of the O10–H16 and N1–H16 internuclear distances in the trajectories of the *Z* isomers of the N3H tautomer: left, starting geometry (black circles); middle, S_1/S_0 hopping point (red triangles); right, final geometry (blue rectangles). The N3H-*tZtc* conformers and ES IPT-related structures are marked by green ellipses. In some trajectories the proton remains on the imidazole ring at the end (green ellipse, right). These trajectories are still in the excited state at the end of the simulation time, which corresponds to $\sim 1\%$ of the total number of simulated trajectories.

was explored in a previous static study[41] could not be identified in any of our dynamics simulations.

Figure 9 addresses the ES IPT process in the *Z* isomers of the N3H tautomer. As described in an earlier study,[41] the excitation to an $n\pi^*$ state (involving a lone-pair MO located at the acid moiety and a π^* MO located mainly on the imidazole ring) will enhance the acidity of the acid moiety and the basicity of the imidazole nitrogen atom by shifting electron density from the acid to the imidazole moiety. This can induce an intramolecular excited-state proton transfer. Figure 9 shows the O10–H16 and N1–H16 distances in the starting geometries of all trajectories of the *Z* isomers of the N3H tautomer (black symbols, left). Here, the N3H-*tZtc* conformer is found at the lower end of the plot (marked by a green ellipse), where the N1–H16 distance is rather short (around 2 Å), indicating the presence of a hydrogen bond between the N1 atom of the imidazole moiety and the H16

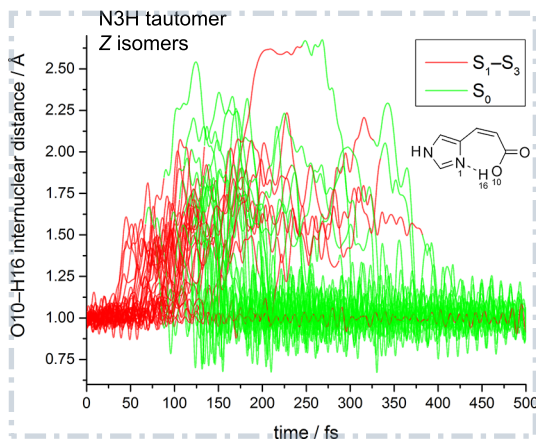


Figure 10: Time evolution of the O10–H16 internuclear distance in 71 selected trajectories of the N3H-*tZtc* conformer during the ESIPT process. Shown are the first 500 fs of the 1.6 ps simulation time. Red and green lines depict the parts of the trajectories evolving in an excited state (S_1 – S_3) and in the ground state (S_0), respectively.

atom of the carboxylic OH group. At the hopping points (red symbols, middle) the lower tail of the curve (green ellipse) represents structures formed by ESIPT, featuring covalent N1–H16 bond lengths (ca. 1 Å) and larger O10–H16 internuclear distances in the hydrogen-bonding range. At the final geometries (blue symbols, right), this lower right tail has almost completely disappeared, because the H16 atom has returned to the O10 atom and the N1–H16 hydrogen bond of roughly 2 Å length has reformed; the few remaining trajectories ($\sim 1\%$) in this tail (green ellipse) have not yet deactivated to the ground state at the end of the simulation (1.6 ps). In two trajectories the proton of the acid moiety has undergone a site exchange within the carboxylic group, which leads to large N1–H16 and O10–H16 distances (red ellipse).

Figure 10 shows the time evolution of the O10–H16 internuclear distance in 71 selected trajectories of the *Z* isomers of the N3H tautomer. In some of these trajectories, the O10–H16 bond length barely changes and only oscillates around its equilibrium value, but in most cases the O10–H16 distance increases sharply. This latter motion starts around 50 fs after excitation and initiates the ESIPT process. Thereafter, deactivation to S_0 can occur readily, sometimes 75 fs and typically 100–150 fs after excitation. After internal conversion to S_0 , the proton moves back to the acid moiety. Figure 10 shows that the fastest trajectories have the proton returned to where it

came from as soon as 100 fs after excitation. Hence, the ESIPT process can be faster than the photoisomerization process. This is to be expected, because ESIPT mainly involves the motion of the migrating proton whereas photoisomerization requires larger distortions of heavy-atom motions.

We also observed ESIPT processes in the reverse direction. For example, in the *Z* isomers of the N1H tautomer the proton moves from the N1H atom of the imidazole ring to the O=C moiety of the acid group (see Fig. S9 in the Supporting Information). We note that the lowest $\pi\pi^*$ excitation leads to a shift in electron density that facilitates this ESIPT, since the π (π^*) MO has more electron density on the imidazole ring (acid moiety). Because of the large number of trajectories undergoing this reverse ESIPT, the *Z* isomers of the N1H tautomer barely isomerize overall (see Fig. 5) and have a very short excited-state lifetime (see Fig. 4).

We also observed such a reverse-direction ESIPT for the C–H→O=C proton transfer (see Fig. S10 in the Supporting Information for a plot on the N1H-*Z* isomers).

The analysis of the prevalence of the ESIPT processes is shown in Figure 11. These histograms were used to count the number of ESIPT events for the *Z* isomers of the two tautomers. Two different types of ESIPT processes are possible in each tautomer (see structural formulas in Fig. 11 and in Figs. 9, S9, S10). The C–H···O → C···H–O process (imidazole moiety to acid moiety) is universal to both tautomers. The second process is an N–H···O → N···H–O process (imidazole to acid) in the N1H tautomer and an O–H···N → O···H–N process (acid to imidazole) in the N3H tautomer. To define a successful occurrence of an ESIPT event, we used the difference in the internuclear distances between the acceptor and H atoms and the donor and H atoms, $d(\text{H}\cdots\text{Y}) - d(\text{X}-\text{H})$, with X being the proton donor and Y being the proton acceptor in the atom triple X–H···Y. If this value becomes negative at the hopping point, the proton is closer to the acceptor atom than it is to the donor atom, in which case we consider a successful ESIPT event to have occurred during the nonadiabatic transition. The histograms in Figure 11 show the counts for the values of the difference in the internuclear distances for the starting structures (black), the S_1/S_0 hopping points (red) and the final structures (green). The bars of negative values for the hopping points (marked by purple rectangles) allow us to count the number of ESIPT events (see text in Fig. 11). The C–H···O → C···H–O process, which is possible in both tautomers, is found for 17% and 14% of trajectories in the N1H and N3H tautomers, respectively. In the N3H tautomer, the O–H···N →

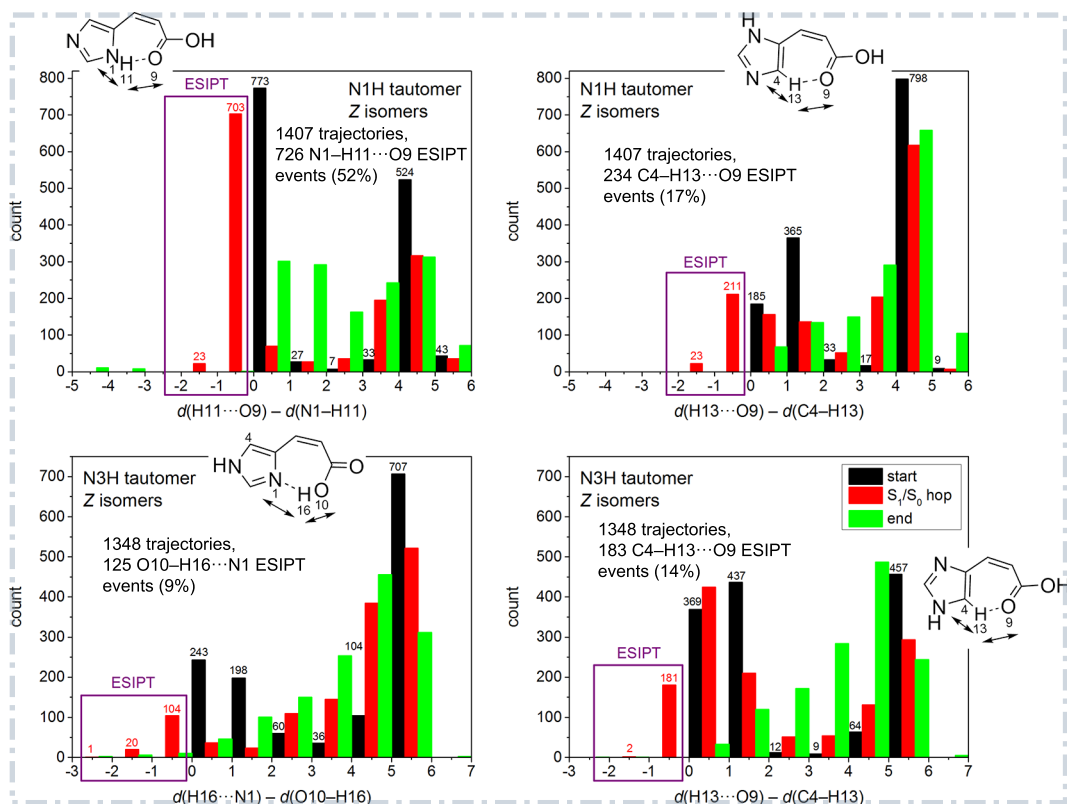


Figure 11: Histograms of the differences in internuclear distances (black: starting geometries; red: S_1/S_0 hopping points; green: final geometries of each trajectory) of each atom triple involved in the two possible ES IPT processes of the Z isomers of each of the two tautomers. The two defining internuclear distances d (see label on x axes) are indicated by double-headed arrows on the structural formulas. A negative difference of the internuclear distances at the S_1/S_0 hopping point indicates that the S_1/S_0 deactivation process involves an ES IPT. The counts for these negative values at the hopping points were used to determine the fraction of trajectories that deactivated via ES IPT; these are marked by purple rectangles. The total fraction of trajectories undergoing ES IPT deactivation is 68% (23%) for the N1H (N3H) tautomer.

$\text{O}\cdots\text{H}-\text{N}$ process is an even rarer event occurring in only 9% of trajectories. The fact that OM2/MRCI underestimates the stability of the N3H- $tZtc$ isomer (see Supporting Information), which is the only isomer capable of this type of ES IPT process, is surely one factor for this low prevalence. All in all, the N3H tautomer undergoes excited-state deactivation via ES IPT by only 23% when the two processes are combined. On the other hand, the N1H tautomer shows a large prevalence for ES IPT via the $\text{N}-\text{H}\cdots\text{O} \rightarrow \text{N}\cdots\text{H}-\text{O}$

process at 52%. In total, the N1H tautomer thus undergoes excited-state deactivation via ESIPT by 68%.

These numbers demonstrate that the *Z* isomers of the N1H tautomer, which show a very low quantum yield for photoisomerization (to be discussed in detail below) of only 16% (see Fig. 5), deactivate predominantly via ESIPT instead. The N3H-*Z* isomers, which show a significantly larger quantum yield for photoisomerization of 48%, deactivate via ESIPT significantly less. In summary, in each of the two tautomers, one of the two competing deactivation mechanisms available in the *Z* isomers dominates strongly over the other one.

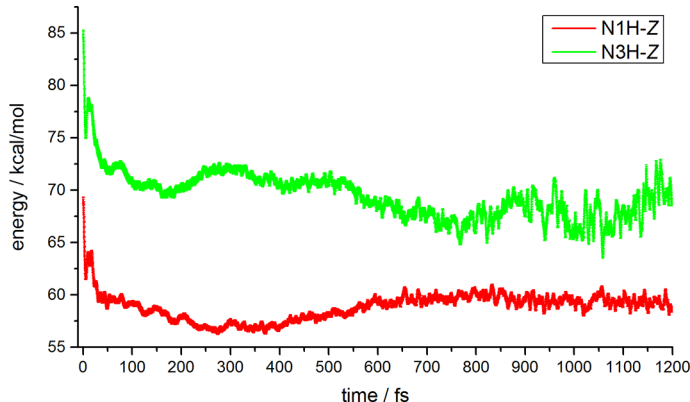


Figure 12: Mean energy (in kcal/mol) at each timestep of the active excited state (S_3 , S_2 or S_1) in all trajectories of the N1H-*Z* (red) and N3H-*Z* (green) isomers within the excited-state segment of each trajectory (i.e. from starting structures to S_1/S_0 hopping points). At early times the averaging includes all simulated trajectories; over time, the number of trajectories included in the averaging decreases as more trajectories have deactivated to S_0 , hence the increase in fluctuations. Shown are the first 1.2 ps of the total simulation time of 1.6 ps.

Why do the *Z* isomers of the N1H tautomer deactivate so predominantly via ESIPT, whereas those of the N3H tautomer do not? Our starting geometries for the *Z* isomers of the two tautomers, which we obtained by randomly sampling from ground-state MD simulations initiated from all possible conformers, mainly consist of the two most stable intramolecularly hydrogen-bonded conformers of each of the tautomers (these are N1H-*tZct*, N1H-*cZct*, N3H-*tZtc*, N3H-*cZct*, see Fig. 2). These two most stable conformers of each tautomer exhibit the very intramolecular hydrogen bond that is the prerequisite for either one of the two possible ESIPT processes in these conformers

(Fig. 11). It is reasonable to assume that the more stable these intramolecularly hydrogen-bonded conformers are, the less likely it is for these species to undergo photoisomerization and the more likely it is for them to undergo ESIPT. Our dynamics data offer some insight into this: Figure S11 in the Supporting Information shows the absolute energies of the $n\pi^*$ and $\pi\pi^*$ states at the starting geometries and at the S_1/S_0 hopping points of the N1H- Z and N3H- Z trajectories. On average, the Z isomers of the N1H tautomer have lower excited-state energies than those of the N3H tautomer, both at the starting geometries and at the hopping points found around 0° . Since practically all of these points represent a structure that exhibits one of the two intramolecular hydrogen bonds required for an ESIPT process, this picture indicates that these structures are more stable in the N1H tautomer than they are in the N3H tautomer. Extending this analysis beyond these two critical points, Figure 12 shows at each timestep the average energy of the active excited state in all the N1H- Z and N3H- Z trajectories within the excited-state segments (i.e. from starting structures to S_1/S_0 hopping points). The excited-state potentials of the N1H tautomer are on average lower in energy than those of the N3H tautomer. In conclusion, the Z isomers of the N1H tautomer are more tightly locked in their Z conformation, which facilitates ESIPT and makes photoisomerization less likely. The Z isomers of the N3H tautomer, on the other hand, are less tightly bound by these intramolecular hydrogen bonds and thus more flexible to undergo photoisomerization.

3.3.4. Quantum Yields for Photoisomerization and for ESIPT

For the following analyses on quantum yields we filtered out the few trajectories that were still in S_1 at the end of the TSH simulations, as it is unknown which photoproducts these trajectories would form when they eventually deactivate to S_0 . Hence, our analyses of quantum yields are based on all those trajectories that have deactivated to S_0 within 1.6 ps.

We computed the photoisomerization quantum yields for the E and Z isomers based on the analyses shown in Figure 5. For both tautomers combined, this gives a quantum yield of 43% for the photoisomerization of the E to Z isomers and of 32% for the reverse process. While the E isomers of the two tautomers show only small differences in the quantum yield for formation of the Z isomers (46% vs. 40% for N1H and N3H), the Z isomers of the two tautomers show very different quantum yields (16 vs. 48% for N1H and N3H). The latter was already rationalized with the different stabilities of the Z isomers of the different tautomers. As shown above, the overall

lower quantum yield for the photoisomerization of Z to E isomers stems from the fact that many of the Z isomers are more or less tightly locked in their conformation by intramolecular hydrogen bonds and, moreover, they have a strong propensity to deactivate via ES IPT rather than photoisomerization.

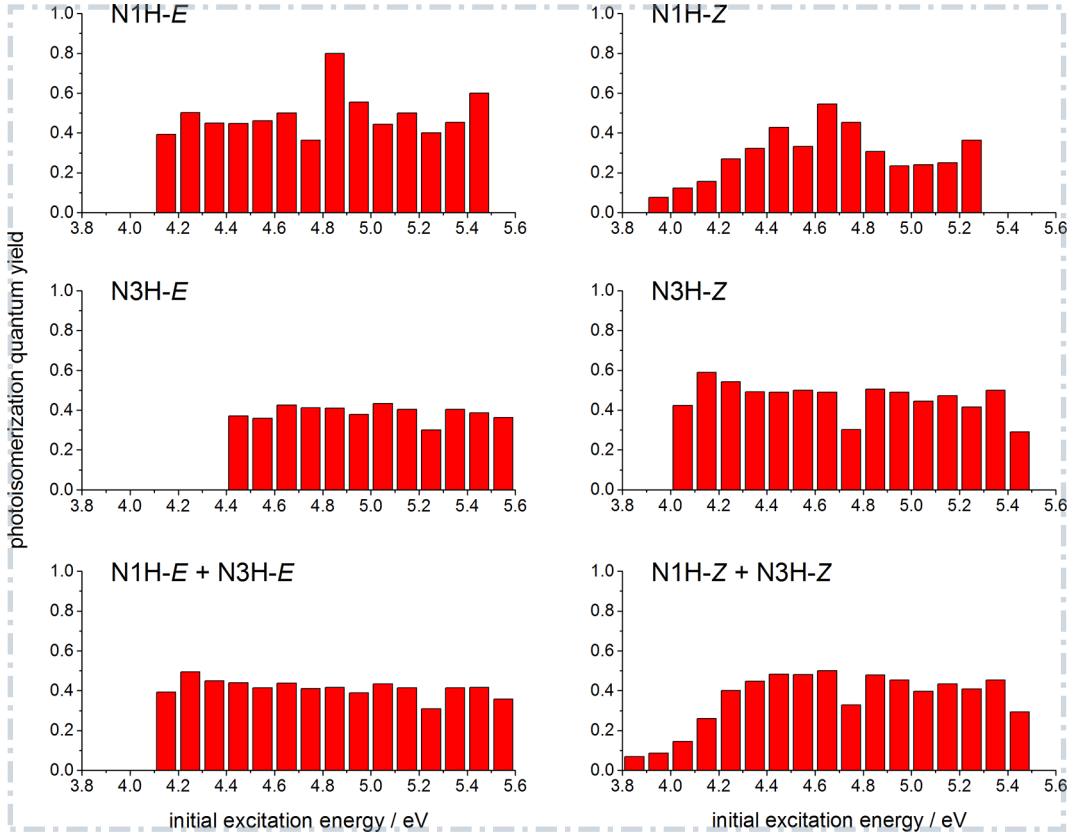


Figure 13: Quantum yield for photoisomerization as a function of the vertical excitation energy of the optically excitable initially populated state at the beginning of each trajectory. Plots are presented for the four classes of isomers used throughout this article and also for all E and Z isomers of both tautomers combined.

To check whether isolated (E)-UA shows an excitation-energy-dependent quantum yield for $E \rightarrow Z$ photoisomerization (EEDQY-PI)[13, 17] we computed the photoisomerization quantum yield as a function of the vertical excitation energy necessary to excite the starting geometry of each trajectory to the initially populated excited state. All bins of the vertical excitation energies with less than ten trajectories were disregarded for this analysis, as the statistical uncertainty would be very large for such small samples. The

resulting plot is shown in Figure 13. For the *E* isomers, we find no significant effect as the quantum yield for photoisomerization stays fairly constant around a value of 0.4 (for both tautomers combined). Only one spike for a quantum yield of 0.8 is visible for the N1H tautomer at an excitation energy of 4.8 eV. Hence, isolated (*E*)-UA does not exhibit an EEDQY-PI (contrary to what was measured in aqueous solution for the *E* isomers, where a change from 0.50 to 0.05 was observed[13, 17]).

Interestingly, the *Z* isomers do show an EEDQY-PI. The photoisomerization quantum yield of the N1H tautomer is very low, around 0.1, at low excitation energies (3.9–4.1 eV), rises to ca. 0.5 for larger excitation energies (4.2–4.7 eV) and then decreases slightly for even larger energies (>4.7 eV). For the *Z* isomers of the N3H tautomer, the quantum yield barely varies with energy, being typically in the range of 0.5, with two dips of 0.3 at 4.7 and 5.4 eV. The plot for the combined N1H and N3H tautomers shows that the *Z* isomers do exhibit an EEDQY-PI. However, this energy dependence appears opposite to the one found experimentally for the *E* isomers in aqueous solution, i.e. the quantum yield increases rather than decreases when going from the lowest to higher excitation energies.

A different presentation of the data for the vertical excitation energies of the initially populated state at the starting geometry and the dihedral angle at the starting and final geometries of each trajectory is given in Figure S12 in the Supporting Information.

The EEDQY-PI found for the *Z* isomers could be connected to the ESIPT mechanism operating in the *Z* isomers. To check on this, we also computed the quantum yields for ESIPT for the *Z* isomers of the two tautomers, to elucidate whether an excitation-energy-dependent quantum yield for ESIPT (EEDQY-ESIPT) exists. These data are presented in Figure 14. The N1H-*Z* isomers indeed show an EEDQY-ESIPT. In the low-energy range, where the quantum yield for photoisomerization increases with higher excitation energies (< 4.4 eV), the quantum yield for ESIPT decreases from 0.9 at 3.6 eV to 0.2 at 4.5 eV excitation energy. After this minimum, the quantum yield rises slightly. Thus, the N1H-*Z* isomers show a complementary behavior in the quantum yields for photoisomerization and ESIPT, which highlights the competition between these two deactivation processes.

The N3H-*Z* isomers, whose quantum yield for photoisomerization was found to be more or less independent of the excitation energy, also show only slight variations in the quantum yield for ESIPT with varying excitation energy, with values found mostly around 0.2–0.3.

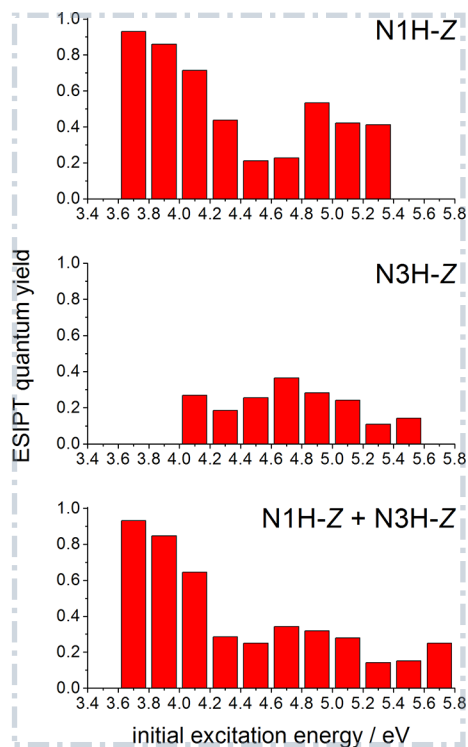


Figure 14: Quantum yield for ES IPT as a function of the vertical excitation energy of the initially populated excited state at the beginning of each trajectory. Plots are presented for the Z isomers of the N1H and N3H tautomers separately and for both tautomers combined.

Figures S13 and S14 in the Supporting Information show histograms of photoisomerization and ES IPT events as a function of the excitation energy.

3.3.5. Summary of Results from the Dynamics Simulations

Table 2 presents a summary of all major quantifiable results obtained from our dynamics simulations, i.e. excited-state lifetimes of the S_2 and S_1 states and the quantum yield for photoisomerization and ES IPT. All these analyses are given for the four classes of isomers separately, for the E and Z isomers of both tautomers combined and for a full mixture of species.

4. Discussion and Conclusions

In this study, we have presented OM2/MRCI TSH simulations of all possible tautomers, isomers and conformers of isolated neutral UA (Fig. 2). We

Table 2: Summary of lifetimes and of quantum yields for photoisomerization and ESIPT for the four classes of isomers and tautomers, for the *E* and *Z* isomers of each tautomer combined and for all species combined.

isomers	S ₂ lifetime / fs	S ₁ lifetime / fs	photoisomerization yield (%)	ESIPT yield (%)
N1H- <i>E</i>	21	408	46	0
N3H- <i>E</i>	13	506	40	0
<i>E</i>	14	459	43	0
N1H- <i>Z</i>	57	337	16	68
N3H- <i>Z</i>	22	271	48	23
<i>Z</i>	30	307	32	46
full mixture	22	373		

▲ have validated the use of OM2/MRCI for the computation of the state order of the low-lying $n\pi^*$ and $\pi\pi^*$ valence excited states for the S₁ and S₂ vertical excitation energies for eight different UA species (tautomers, *E/Z* isomers and conformers). The physical character of the S₁ and S₂ states is correctly reproduced by OM2/MRCI (Table S1 in the Supporting Information). The characteristic qualitative shape of the S₁ and S₂ excited-state potential-energy surfaces along the photoisomerization coordinate is also well described by OM2/MRCI. This has been shown by mapping the critical points (starting geometries, S₁/S₀ hopping points and final geometries) of the excited-state trajectories onto the photoisomerization coordinate space (Fig. 8).

The initial conditions for the dynamics simulations were generated by 1 ns ground-state SCC-DFTB MD simulations, which were performed for each possible conformer of the *E* and *Z* isomers of each tautomer of UA (Fig. 2). From these 32 MD trajectories, 8000 structures were randomly sampled and filtered for initial conditions by computing VEEs and oscillator strengths to determine for each structure the bright state(s) most likely to be populated via optical excitation. Almost 6000 initial conditions were obtained in this manner (Table 1, Fig. 3), which served as starting points for the OM2/MRCI TSH simulations.

The computed S₁ lifetimes are in the range 271–506 fs (Fig. 4) while the S₂ state is much shorter-lived (13–57 fs). The *Z* isomers deactivate faster than the *E* isomers. The S₁ population of the *E* isomers does not reach 0, as observed for the *Z* isomers, but reaches a plateau value of 0.06 and 0.05 for the N1H and N3H tautomers, respectively.

The TSH simulations showed that the *E* isomers of UA photoisomerize more readily than the *Z* isomers. The quantum yield for photoisomerization was found to be 43% for the *E* isomers, compared to only 32% for the *Z* isomers (Fig. 5). This was rationalized by the propensity of the *Z* isomers to form intramolecular hydrogen bonds (Fig. 6), which lock them in the *Z* conformation and thus restrain torsional motions towards the *E* isomer. Most notably we found a large difference in the quantum yields for photoisomerization for the *Z* isomers of the N1H and N3H tautomers (16 vs. 48%). We found that the excited-state energies of the N1H-*Z* isomers are lower than those of the N3H-*Z* isomers (Figs. S11, 12), which suggests that the intramolecular hydrogen bonds in the N1H-*Z* isomers are stronger than in the N3H-*Z* isomers. Stronger intramolecular hydrogen bonds inhibit the flexibility of the *Z* isomers required for successful photoisomerization and thus lead to a higher quantum yield for ESIPT.

Ultrafast ESIPT processes are possible in all of the most stable conformers of *Z* isomers, but not in the *E* isomers. The deactivation via ESIPT can normally be completed within 50–200 fs after excitation (Fig. 10), whereas via photoisomerization it typically takes 100–400 fs to reach the S_1/S_0 conical-intersection seam (Fig. 7). Hence, the *Z* isomers can show a strong preference to deactivate via ESIPT rather than via photoisomerization and they can do so faster than the *E* isomers. In the dynamics simulations, ESIPT processes (in both directions for the N3H tautomer) were observed (Figs. 9, S9, S10) for two types of intramolecular hydrogen bonds (Fig. 11) found in the different conformers of the *Z* isomers (Fig. 2). Overall, the ESIPT processes in the *Z* isomers contribute to their shorter excited-state lifetimes and their lower quantum yields for photoisomerization. Surprisingly, however, despite the strong tendency for intramolecular hydrogen bonds, the N3H-*Z* isomers gave a larger quantum yield for photoisomerization than even the *E* isomers (48% for N3H-*Z* vs. 40% for N1H-*E* and 46% for N3H-*E*). The quantum yields for ESIPT (Fig. 11) were found at 68% for the N1H tautomer, consistent with its low quantum yield for photoisomerization. The N3H tautomer, which photoisomerizes significantly, correspondingly shows a low quantum yield for ESIPT of only 23%.

We could not find evidence for an excitation-energy-dependent quantum yield for photoisomerization (EEDQY-PI) in isolated (*E*)-UA (Fig. 13). The present simulations thus do not offer support for previous hypotheses that the EEDQY-PI could be rooted in the different absorption spectra of the tautomers[40] or in the different order of the two lowest excited

states of the tautomers.[41] The same applies to earlier suggestions that the EEDQY-PI might be caused by two electronic states with overlapping absorption spectra[16, 26] or arise from multiple ground-state rotamers.[16] On the contrary, the current results suggest that the EEDQY-PI does not exist in isolated (*E*)-UA and should thus be an effect that develops in aqueous solution.[13, 17] However, we did observe an EEDQY-PI in the case of the N1H-*Z* isomers: the quantum yield is low for low excitation energies and higher for larger excitation energies. This is opposite to the energy dependence that has been experimentally observed for (*E*)-UA in aqueous solution.[13, 17] We also found a distinct excitation-energy-dependent quantum yield for ESIPT (EEDQY-ESIPT) in the N1H-*Z* isomers (Fig. 14), which is complementary to its EEDQY-PI in the lower ranges of excitation energies. The N3H-*Z* isomers, on the other hand, show only minor variations in the quantum yield for ESIPT (as they do also for photoisomerization).

Surprisingly, although the excited-state deactivation of the *Z* isomers is clearly driven by two competing processes—photoisomerization and ESIPT—we could not find evidence for biexponential decay of the excited-state populations. Our attempts at fitting a biexponential decay function to the S_1 population curve failed. Plotting the natural logarithm of the S_1 population against time also does not reveal the existence of two processes of different deactivation speeds in the form of a pronounced kink in the line. This suggests that on average both photoisomerization and ESIPT processes operate in the same range of timescales from as fast as 50 fs to as slow as 500 fs, thus resulting in monoexponential decay. The computed excited-state lifetime of ~ 475 fs for the combined *E* isomers of the N1H and N3H tautomers (S_1+S_2 , Fig. S6) could be compared with a fs-laser-spectroscopic determination of the excited-state lifetime of gas-phase UA, which could be conducted using commercially available (*E*)-UA (a mixture of N1H and N3H tautomers).

According to our OM2/MRCI TSH simulations, ESIPT should be the dominating deactivation process in the *Z* isomers. In the N3H tautomer, such a proton transfer is not only possible in the direction acid moiety \rightarrow imidazole ring (as previously explored[41]), but also in the opposite direction. Having observed that the N–H and even the C–H group of the imidazole ring can act as a proton donor raises the question whether this is indeed true or whether OM2/MRCI erroneously overestimates the photoacidity of the annular N–H and C–H bonds. This issue may be resolved in future theoretical studies by exploring the excited-state dynamics of UA with multiconfigurational *ab initio* methods.[49, 81]

Furthermore, this study has laid the groundwork for future excited-state dynamics simulations of UA in an aqueous surrounding. Such simulations could elucidate whether the EEDQY-PI found experimentally in aqueous solution[13, 17] can be reproduced computationally. Also, our finding of a complementary behavior of the EEDQY-PI and EEDQY-ESIPT in the N1H-Z isomers raises the question of whether there is also an excitation-energy-dependent quantum yield for proton transfer in the *E* isomers, which is complementary to the EEDQY-PI measured in water.[13, 17] In this case, however, the proton would not be intramolecularly transferred, as studied herein, but between UA and surrounding water molecules.


Finally, in practical terms, this study is a good example for the capabilities of the OM2/MRCI method for excited-state dynamics simulations. We have simulated almost 6000 excited-state trajectories of 1.6 ps length at a regular timestep of 0.2 fs, with a typical runtime of 3–4 hours on a single contemporary CPU. Hence, all these trajectories can be run in a few days when using ~100 CPUs in parallel. The statistical analysis of such a large number of trajectories leads to well-converged results and allows detailed insight not only into the dominant photoinduced processes but also into side events. In addition, as exemplified here for the case of UA, the high efficiency of the OM2/MRCI TSH approach enables comprehensive dynamics studies of all relevant tautomers, isomers and conformers.


Acknowledgement


This work was supported by the European Research Council through an ERC Advanced Grant to W.T. (OMSQC). M.B. acknowledges support from the Excellence Initiative of Aix-Marseille University (A*MIDEX) and the project Equip@Meso (ANR-10-EQPX-29-01), both funded by the “Investissements d’Avenir” program of the French Government, as well as from the WSPLIT project (ANR-17-CE05-0005-01). D.T.: I am highly grateful for the guidance, support and experience that I enjoyed during my time in Wolfgang Domcke’s research group. Urocanic acid was the first molecule that Wolfgang Domcke suggested as a potential subject of study to me and it has been a focus of my scientific interests ever since.

References


- [1] T. Mohammad, H. Morrison, H. HogenEsch, Urocanic acid photochemistry and photobiology., *Photochem. Photobiol.* 69 (1999) 115–135.

- [2] J. D. Simon, Spectroscopic and dynamic studies of the epidermal chromophores *trans*-urocanic acid and eumelanin., *Acc. Chem. Res.* 33 (2000) 307–313.
- [3] N. K. Gibbs, J. Tye, M. Norval, Recent advances in urocanic acid photochemistry, photobiology and photoimmunology., *Photochem. Photobiol. Sci.* 7 (2008) 655–667. 
- [4] N. K. Gibbs, M. Norval, Urocanic acid in the skin: a mixed blessing?, *J. Invest. Dermatol.* 131 (2011) 14–17.
- [5] H. C. Arentsen, C. F. J. Jansen, C. A. Hulsbergen-van de Kaa, J. K. Laihia, L. Pylkkänen, L. Leino, E. Oosterwijk, J. A. Witjes, Antitumor effects of *cis*-urocanic acid on experimental urothelial cell carcinoma of the bladder., *J. Urol.* 187 (2012) 1445–1449.
- [6] G. M. Arocena, A. Zorreguieta, R. Sieira, Expression of VjbR under nutrient limitation conditions is regulated at the post-transcriptional level by specific acidic pH values and urocanic acid., *PLoS One* 7 (2012) 1–9.
- [7] T. Yamaguchi, K. Hiromasa, R. Kabashima-Kubo, M. Yoshioka, M. Nakamura, Galectin-7, induced by *cis*-urocanic acid and ultraviolet B irradiation, down-modulates cytokine production by T lymphocytes., *Exp. Dermatol.* 22 (2013) 840–842.
- [8] N. E. Wezynfeld, W. Goch, W. Bal, T. Fraczyk, *cis*-Urocanic acid as a potential nickel(II) binding molecule in the human skin., *Dalton Trans.* 43 (2014) 3196–3201.
- [9] J. E. Ihm, I. Krier, J. M. Lim, S. Shim, D. K. Han, J. A. Hubbell, Improved biocompatibility of polyethylenimine (PEI) as a gene carrier by conjugating urocanic acid: *In vitro* and *in vivo.*, *Macromol. Res.* 23 (2015) 387–395.
- [10] E. Korhonen, N. Piippo, M. Hytti, K. Kaarniranta, A. Kauppinen, *cis*-Urocanic acid prevents inflammation and cell death in UVB-treated ARPE-19 cells., *Acta Ophthalmol.* 93 (2015) 0427.


- [11] B. Xiao, P. Ma, E. Viennois, D. Merlin, Urocanic acid-modified chitosan nanoparticles can confer anti-inflammatory effect by delivering CD98 siRNA to macrophages., *Colloids Surf. B* 143 (2016) 186 – 193.
- [12] D. L. Pham, K.-M. Lim, K.-M. Joo, H.-S. Park, D. Y. M. Leung, Y.-M. Ye, Increased *cis*-to-*trans* urocanic acid ratio in the skin of chronic spontaneous urticaria patients., *Sci. Rep.* 7 (2017) 1318. 
- [13] H. Morrison, C. Bernasconi, G. Pandey, A wavelength effect on urocanic acid *E/Z* photoisomerization., *Photochem. Photobiol.* 40 (1984) 549–550.
- [14] J. K. Laihia, H. Lemmetyinen, P. Pasanen, C. T. Jansén, Establishment of a kinetic model for urocanic acid photoisomerization., *J. Photochem. Photobiol. B* 33 (1996) 211–217.
- [15] B. Li, K. M. Hanson, J. D. Simon, Primary processes of the electronic excited states of *trans*-urocanic acid., *J. Phys. Chem. A* 101 (1997) 969–972.
- [16] K. M. Hanson, B. Li, J. D. Simon, A spectroscopic study of the epidermal ultraviolet chromophore *trans*-urocanic acid., *J. Am. Chem. Soc.* 119 (1997) 2715–2721.
- [17] K. M. Hanson, J. D. Simon, The origin of the wavelength-dependent photoreactivity of *trans*-urocanic acid., *Photochem. Photobiol.* 67 (1998) 538–540.
- [18] A. Kammeyer, T. A. Eggelte, J. D. Bos, M. B. M. Teunissen, Urocanic acid isomers are good hydroxyl radical scavengers: a comparative study with structural analogues and with uric acid., *Biochim. Biophys. Acta* 1428 (1999) 117–120.
- [19] N. Haralampus-Grynaviski, C. Ransom, T. Ye, M. Rôzanowska, M. Wrona, T. Sarna, J. D. Simon, Photogeneration and quenching of reactive oxygen species by urocanic acid., *J. Am. Chem. Soc.* 124 (2002) 3461–3468.
- [20] J. Brookman, J. N. Chaçon, R. S. Sinclair, Some photophysical studies of *cis*- and *trans*-urocanic acid., *Photochem. Photobiol. Sci.* 1 (2002) 327–332.

- [21] E. L. Menon, H. Morrison, Formation of singlet oxygen by urocanic acid by UVA irradiation and some consequences thereof., *Photochem. Photobiol.* 75 (2002) 565–569.
- [22] B. Schwarzingler, H. Falk, Concerning the photodiastereomerization and protic equilibria of urocanic acid and its complex with human serum albumin., *Monatsh. Chem.* 135 (2004) 1297–1304. 
- [23] R. A. Wallis, G. J. Smith, C. L. Dunford, The effect of molecular environment on the photoisomerization of urocanic acid., *Photochem. Photobiol.* 80 (2004) 257–261.
- [24] J. Baier, T. Maisch, E. Engel, M. Landthaler, W. Bäumlner, Singlet oxygen generation by UVA light exposure of endogenous photosensitizers., *Biophys. J.* 91 (2006) 1452–1459.
- [25] M. Egawa, J. Nomura, H. Iwaki, The evaluation of the amount of *cis*- and *trans*-urocanic acid in the stratum corneum by Raman spectroscopy., *Photochem. Photobiol. Sci.* 9 (2010) 730–733.
- [26] W. L. Ryan, D. H. Levy, Electronic spectroscopy and photoisomerization of *trans*-urocanic acid in a supersonic jet., *J. Am. Chem. Soc.* 123 (2001) 961–966.
- [27] M. K. Shukla, P. C. Mishra, Electronic spectra, structure and photoisomerization of urocanic acid., *Spectrochim. Acta* 51A (1995) 831–838.
- [28] A. Lahti, M. Hotokka, K. Neuvonen, P. Äyräs, A theoretical study of the conformers of *trans*- and *cis*-urocanic acid., *J. Mol. Struct.: THEOCHEM* 331 (1995) 169–179.
- [29] A. Lahti, M. Hotokka, K. Neuvonen, P. Äyräs, Quantum-chemical gas-phase calculations on the protonation forms of *trans*- and *cis*-urocanic acid., *Struct. Chem.* 8 (1997) 331–342.
- [30] A. Lahti, M. Hotokka, K. Neuvonen, G. Karlström, Quantum chemical calculations on the intramolecular hydrogen bond of *cis*-urocanic acid., *J. Mol. Struct.: THEOCHEM* 452 (1998) 185–202.
- [31] A. Lahti, M. Hotokka, K. Neuvonen, G. Karlström, A CASSCF study on the lowest $\pi \rightarrow \pi^*$ excitation of urocanic acid., *Int. J. Quant. Chem.* 72 (1999) 25–37.

- [32] C. S. Page, M. Merchán, L. Serrano-Andrés, M. Olivucci, A theoretical study of the low-lying excited states of *trans*- and *cis*-urocanic acid., J. Phys. Chem. A 103 (1999) 9864–9871.
- [33] C. S. Page, M. Olivucci, M. Merchán, A theoretical study of the low-lying states of the anionic and protonated ionic forms of urocanic acid., J. Phys. Chem. A 104 (2000) 8796–8805. [▲](#)
- [34] J. Danielsson, J. Uličný, A. Laaksonen, A TD-DFT study of the photochemistry of urocanic acid in biologically relevant ionic, rotameric, and protomeric forms., J. Am. Chem. Soc. 123 (2001) 9817–9821.
- [35] J. Danielsson, J. A. Söderhall, A. Laaksonen, Hydration structure and conformational dynamics of urocanic acid: a computer simulation study., Mol. Phys. 100 (2002) 1873–1886.
- [36] J. Danielsson, A. Laaksonen, Gas phase photoisomerization of urocanic acid – a theoretical study., Chem. Phys. Lett. 370 (2003) 625–630.
- [37] O. Dmitrenko, W. Reischl, R. D. Bach, J. Spanget-Larsen, TD-DFT computational insight into the origin of wavelength-dependent *E/Z* photoisomerization of urocanic acid., J. Phys. Chem. A 108 (2004) 5662–5669.
- [38] L. Shen, H.-F. Ji, Theoretical investigation of the photosensitization mechanisms of urocanic acid., J. Photochem. Photobiol. B 91 (2008) 96–98.
- [39] S. Tiwari, P. C. Mishra, Urocanic acid as an efficient hydroxyl radical scavenger: a quantum theoretical study., J. Mol. Model. 17 (2011) 59–72.
- [40] M. Barbatti, The role of tautomers in the UV absorption of urocanic acid., Phys. Chem. Chem. Phys. 13 (2011) 4686–4692.
- [41] D. Tuna, A. L. Sobolewski, W. Domcke, Photochemical mechanisms of radiationless deactivation processes in urocanic acid., J. Phys. Chem. B 118 (2014) 976–985.
- [42] W. Weber, W. Thiel, Orthogonalization corrections for semiempirical methods., Theor. Chem. Acc. 103 (6) (2000) 495–506.

- [43] W. Thiel, Semiempirical quantum-chemical methods., WIREs Comput. Mol. Sci. 4 (2014) 145–157.
- [44] P. O. Dral, X. Wu, L. J. Spörkel, A. Kosłowski, W. Weber, R. Steiger, M. Scholten, W. Thiel, Semiempirical quantum-chemical orthogonalization-corrected methods: theory, implementation, and parameters., J. Chem. Theory Comput. 12 (2016) 1082–1096. 
- [45] A. Kosłowski, M. E. Beck, W. Thiel, Implementation of a general multireference configuration interaction procedure with analytic gradients in a semiempirical context using the graphical unitary group approach., J. Comput. Chem. 24 (2003) 714–726.
- [46] D. Tuna, Y. Lu, A. Kosłowski, W. Thiel, Semiempirical quantum-chemical orthogonalization-corrected methods: benchmarks of electronically excited states., J. Chem. Theory Comput. 12 (2016) 4400–4422.
- [47] B. G. Levine, T. J. Martínez, Isomerization through conical intersections., Annu. Rev. Phys. Chem. 58 (2007) 613–634.
- [48] A. Nenov, T. Cordes, T. T. Herzog, W. Zinth, R. de Vivie-Riedle, Molecular driving forces for Z/E isomerization mediated by heteroatoms: the example hemithioindigo., J. Phys. Chem. A 114 (2010) 13016–13030.
- [49] L. Liu, J. Liu, T. J. Martínez, Dynamical correlation effects on photoisomerization: ab initio multiple spawning dynamics with MS-CASPT2 for a model *trans*-protonated Schiff base., J. Phys. Chem. B 120 (2016) 1940–1949.
- [50] S. Gozem, H. L. Luk, I. Schapiro, M. Olivucci, Theory and simulation of the ultrafast double-bond isomerization of biological chromophores., Chem. Rev. 117 (22) (2017) 13502–13565.
- [51] A. L. Sobolewski, W. Domcke, *Ab initio* potential-energy functions for excited state intramolecular proton transfer: a comparative study of *o*-hydroxybenzaldehyde, salicylic acid and 7-hydroxy-1-indanone., Phys. Chem. Chem. Phys. 1 (1999) 3065–3072.
- [52] M. J. Paterson, M. A. Robb, L. Blancafort, A. D. DeBellis, Theoretical study of benzotriazole uv photostability: ultrafast deactivation

- through coupled proton and electron transfer triggered by a charge-transfer state., *J. Am. Chem. Soc.* 126 (2004) 2912–2922.
- [53] J. D. Coe, B. G. Levine, T. J. Martínez, Ab initio molecular dynamics of excited-state intramolecular proton transfer using multireference perturbation theory., *J. Phys. Chem. A* 111 (2007) 11302–11310.
- [54] J. Jankowska, M. Barbatti, J. Sadlej, A. L. Sobolewski, Tailoring the Schiff base photoswitching – a non-adiabatic molecular dynamics study of substituent effect on excited state proton transfer., *Phys. Chem. Chem. Phys.* 19 (2017) 5318–5325.
- [55] J. C. Tully, Molecular dynamics with electronic transitions., *J. Chem. Phys.* 93 (1990) 1061–1071.
- [56] M. Barbatti, Nonadiabatic dynamics with trajectory surface hopping method., *WIREs Comput. Mol. Sci.* 1 (2011) 620–633.
- [57] E. Tapavicza, G. D. Bellchambers, J. C. Vincent, F. Furche, *Ab initio* non-adiabatic molecular dynamics., *Phys. Chem. Chem. Phys.* 15 (2013) 18336–18348.
- [58] B. F. E. Curchod, U. Rothlisberger, I. Tavernelli, Trajectory-based nonadiabatic dynamics with time-dependent density functional theory., *ChemPhysChem* 14 (2013) 1314–1340.
- [59] J. E. Subotnik, A. Jain, B. Landry, A. Petit, W. Ouyang, N. Bellonzi, Understanding the surface hopping view of electronic transitions and decoherence., *Annu. Rev. Phys. Chem.* 67 (1) (2016) 387–417.
- [60] L. Spörkel, J. Jankowska, W. Thiel, Photoswitching of salicylidene methylamine: a theoretical photodynamics study., *J. Phys. Chem. B* 119 (2015) 2702–2710.
- [61] A. Nikiforov, J. A. Gámez, W. Thiel, M. Filatov, Computational design of a family of light-driven rotary molecular motors with improved quantum efficiency., *J. Phys. Chem. Lett.* 7 (2016) 105–110.
- [62] X.-Y. Liu, X.-P. Chang, S.-H. Xia, G. Cui, W. Thiel, Excited-state proton-transfer-induced trapping enhances the fluorescence emission of a locked GFP chromophore., *J. Chem. Theory Comput.* 12 (2016) 753–764.

- [63] Y.-T. Wang, X.-Y. Liu, G. Cui, W.-H. Fang, W. Thiel, Photoisomerization of arylazopyrazole photoswitches: stereospecific excited-state relaxation., *Angew. Chem. Int. Ed.* 55 (2016) 14009–14013.
- [64] Y.-J. Gao, X.-P. Chang, X.-Y. Liu, Q.-S. Li, G. Cui, W. Thiel, Excited-state decay paths in tetraphenylethene derivatives., *J. Phys. Chem. A* 121 (13) (2017) 2572–2579. 
- [65] W. Thiel, MNDO99 program, version 6.1. 2007; Max-Planck-Institut für Kohlenforschung: Mülheim, Germany, 2007. Available from the author upon private communication.
- [66] TURBOMOLE V6.3.1 2011, a development of University of Karlsruhe and Forschungszentrum Karlsruhe GmbH, 1989-2007, TURBOMOLE GmbH, since 2007, available from <http://www.turbomole.com>.
- [67] ChemShell, a Computational Chemistry Shell, see www.chemshell.org.
- [68] S. Metz, J. Kästner, A. A. Sokol, T. W. Keal, P. Sherwood, Chemshell—a modular software package for QM/MM simulations., *WIREs Comput. Mol. Sci.* 4 (2014) 101–110.
- [69] G. Granucci, M. Persico, Critical appraisal of the fewest switches algorithm for surface hopping., *J. Chem. Phys.* 126 (13) (2007) 134114.
- [70] L. Spörkel, W. Thiel, Adaptive time steps in trajectory surface hopping simulations., *J. Chem. Phys.* 144 (2016) 194108.
- [71] W. Domcke, D. R. Yarkony, H. Köppel (Eds.), *Conical Intersections: Electronic Structure, Dynamics & Spectroscopy*, World Scientific Publishing, Singapore, 2004.
- [72] W. Domcke, D. R. Yarkony, H. Köppel (Eds.), *Conical Intersections: Theory, Computation and Experiment*, World Scientific Publishing, Singapore, 2011.
- [73] M. Barbatti, M. Ruckebauer, J. J. Szymczak, A. J. A. Aquino, H. Lischka, Nonadiabatic excited-state dynamics of polar π -systems and related model compounds of biological relevance., *Phys. Chem. Chem. Phys.* 10 (2008) 482–494.

- [74] M. Elstner, D. Porezag, G. Jungnickel, J. Elsner, M. Haugk, T. Frauenheim, S. Suhai, G. Seifert, Self-consistent-charge density-functional tight-binding method for simulations of complex materials properties., *Phys. Rev. B* 58 (1998) 7260–7268.
- [75] M. Barbatti, G. Granucci, M. Persico, M. Ruckebauer, M. Vazdar, M. Eckert-Maksić, H. Lischka, The on-the-fly surface-hopping program system Newton-X: application to ab initio simulation of the nonadiabatic photodynamics of benchmark systems., *J. Photochem. Photobiol. A* 190 (2) (2007) 228 – 240.
- [76] S. Ameer-Beg, S. M. Ormson, R. G. Brown, P. Matousek, M. Towrie, E. T. J. Nibbering, P. Foggi, F. V. R. Neuwahl, Ultrafast measurements of excited state intramolecular proton transfer (ESIPT) in room temperature solutions of 3-hydroxyflavone and derivatives., *J. Phys. Chem. A* 105 (2001) 3709–3718.
- [77] S. Lochbrunner, A. J. Wurzer, E. Riedle, Microscopic mechanism of ultrafast excited-state intramolecular proton transfer: a 30-fs study of 2-(2'-hydroxyphenyl)benzothiazole., *J. Phys. Chem. A* 107 (2003) 10580–10590.
- [78] P. K. Verma, A. Steinbacher, F. Koch, P. Nuernberger, T. Brixner, Monitoring ultrafast intramolecular proton transfer processes in an unsymmetric β -diketone., *Phys. Chem. Chem. Phys.* 17 (2015) 8459–8466.
- [79] S. Pijeu, D. Foster, E. G. Hohenstein, Excited-state dynamics of a benzotriazole photostabilizer: 2-(2'-hydroxy-5'-methylphenyl)benzotriazole, *J. Phys. Chem. A* 121 (2017) 6377–6387.
- [80] H. Böhnke, J. Bahrenburg, X. Ma, K. Röttger, C. Näther, M. F. Rode, A. L. Sobolewski, F. Temps, Ultrafast dynamics of the ESIPT photoswitch *N*-(3-pyridinyl)-2-pyridinecarboxamide., *Phys. Chem. Chem. Phys.* 20 (2018) 2646–2655.
- [81] J. W. Park, T. Shiozaki, On-the-fly CASPT2 surface-hopping dynamics., *J. Chem. Theory Comput.* 13 (2017) 3676–3683.